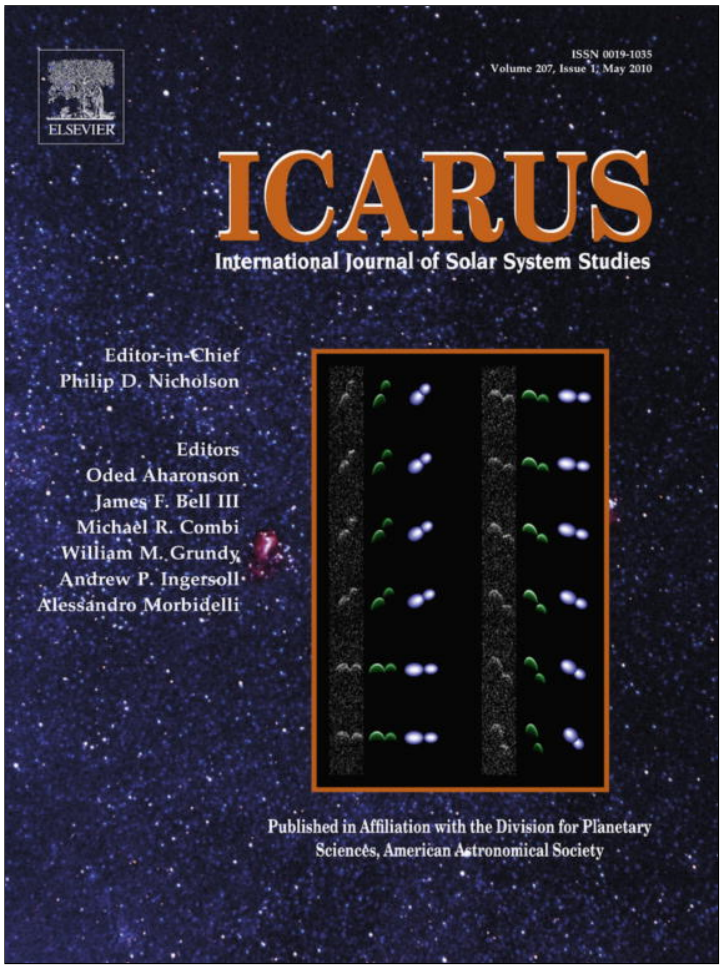

Icarus 207 (2010) 394–408

Contents lists available at ScienceDirect

Icarus

journal homepage: www.elsevier.com/locate/icarus

# Multi-wavelength simulations of atmospheric radiation from Io with a 3-D spherical-shell backward Monte Carlo radiative transfer model

Sergey L. Gratiy [a,*], Andrew C. Walker [b], Deborah A. Levin [a], David B. Goldstein [b], Philip L. Varghese [b], Laurence M. Trafton [b], Chris H. Moore [b]

[a] Department of Aerospace Engineering, Pennsylvania State University, University Park, PA 16802, USA
[b] Department of Aerospace Engineering, University of Texas at Austin, Austin, TX 78712, USA

ARTICLE INFO

*Article history:*
Received 19 June 2009
Revised 29 October 2009
Accepted 4 November 2009
Available online 26 November 2009

*Keywords:*
Radiative transfer
Io
Atmospheres, Dynamics
Atmospheres, Structure
Satellites, Atmospheres

ABSTRACT

Conflicting observations regarding the dominance of either sublimation or volcanism as the source of the atmosphere on Io and disparate reports on the extent of its spatial distribution and the absolute column abundance invite the development of detailed computational models capable of improving our understanding of Io's unique atmospheric structure and origin. Improving upon previous models, Walker et al. (Walker, A.C., Gratiy, S.L., Levin, D.A., Goldstein, D.B., Varghese, P.L., Trafton, L.M., Moore, C.H., Stewart, B. [2009]. Icarus) developed a fully 3-D global rarefied gas dynamics model of Io's atmosphere including both sublimation and volcanic sources of $SO_2$ gas. The fidelity of the model is tested by simulating remote observations at selected wavelength bands and comparing them to the corresponding astronomical observations of Io's atmosphere. The simulations are performed with a new 3-D spherical-shell radiative transfer code utilizing a backward Monte Carlo method. We present: (1) simulations of the mid-infrared disk-integrated spectra of Io's sunlit hemisphere at 19 μm, obtained with TEXES during 2001–2004; (2) simulations of disk-resolved images at Lyman-α obtained with the Hubble Space Telescope (HST), Space Telescope Imaging Spectrograph (STIS) during 1997–2001; and (3) disk-integrated simulations of emission line profiles in the millimeter wavelength range obtained with the IRAM-30 m telescope in October–November 1999. We found that the atmospheric model generally reproduces the longitudinal variation in band depth from the mid-infrared data; however, the best match is obtained when our simulation results are shifted ∼30° toward lower orbital longitudes. The simulations of Lyman-α images do not reproduce the mid-to-high latitude bright patches seen in the observations, suggesting that the model atmosphere sustains columns that are too high at those latitudes. The simulations of emission line profiles in the millimeter spectral region support the hypothesis that the atmospheric dynamics favorably explains the observed line widths, which are too wide to be formed by thermal Doppler broadening alone.



## 1. Introduction

The *Voyager 1* spacecraft discovery of active volcanism on Io in 1979 revealed Io as the most active body in the Solar System and earned it a unique place among planetary satellites (Morabito et al., 1979). The same year the infrared imaging spectrograph (IRIS) onboard *Voyager* detected gaseous $SO_2$ over the volcanic center Loki Patera at 7.3 μm (Pearl et al., 1979). The spectra were consistent with column densities of (2.5–20) × $10^{17}$ $cm^{-2}$ and temperatures of up to 400 K (Lellouch et al., 1992). The detection of $SO_2$ as a gas helped to attribute a previously unidentified infrared spectral absorption feature at 4.07 μm to solid $SO_2$, lending to the hypothesis that the atmosphere of Io may be supported by frost sublimation as much as by active volcanism.

Numerous observations obtained since 1990 provide consistent evidence that Io has a tenuous but collisionally thick global atmosphere dominated by $SO_2$ gas. The atmospheric structure was found to exhibit dramatic lateral variations and a limited temporal variability. Spatially resolved HST Faint Object Spectrograph (FOS) observations of the volcanic center Ra (7°S, 318°W) covering the spectral region 1590–2312 Å indicate a column density of 1.5 × $10^{16}$ $cm^{-2}$ (McGrath et al., 2000). In contrast, Jessup et al. (2004) using 2000–3000 Å disk-resolved spectroscopy from HST/STIS inferred column densities of 1.25 × $10^{17}$ $cm^{-2}$ near the subsolar point at longitude 162°W – eight times the value determined for Ra, indicating a strong longitudinal variability. The same observations revealed a strong latitudinal variation on the anti-jovian hemisphere with column density dropping below 2 × $10^{16}$ $cm^{-2}$ for latitudes beyond ±50°.

Clear evidence for strong longitudinal asymmetries of atmospheric abundance was provided by the ground-based

* Corresponding author.
*E-mail address:* slg284@psu.edu (S.L. Gratiy).

0019-1035/$ - see front matter © 2009 Elsevier Inc. All rights reserved.
doi:10.1016/j.icarus.2009.11.004

observations of the sunlit hemisphere of Io with the TEXES high resolution mid-infrared spectrograph at the NASA Infrared Telescope Facility (IRTF), conducted during 2001–2004 (Spencer et al., 2005). The observations include a set of disk-integrated absorption spectra at 19 μm taken at different orbital longitudes of Io. The most plausible interpretation of the spectra indicated that the equatorial column density varies from $\sim 1.5 \times 10^{17}$ cm$^{-2}$ near a longitude of 180°W to $\sim 1.5 \times 10^{16}$ cm$^{-2}$ near a longitude of 300°W.

The most detailed evidence for the latitudinal variation of the atmospheric abundance at spatial resolution ~200 km is inferred from the HI Lyman-α (1216 Å) images of Io obtained with HST/STIS during 1997–2001 (Roesler et al., 1999; Feaga et al., 2009). The images show bright patches (~2 kR) at mid-to-high latitudes and much darker patches (~0.7 kR) at equatorial latitudes. The interpretation of this data by Feldman et al. (2000) and Strobel and Wolven (2001) indicated a strong latitudinal fall-off in $SO_2$ column densities, suggesting that the atmosphere on Io is restricted to a 30–40° band north and south of the equator with modest longitudinal inhomogeneities.

Evidence of significant latitudinal and longitudinal variability in the atmospheric abundance and uncertainties regarding the extent of the atmospheric coverage raise a principal question: what is the relative role of the surface frost sublimation and volcanoes in supporting the immediate atmosphere on Io? This question is essential in terms of the vertical structure, lifetime, response to insolation variation, and chemical composition. A sublimation atmosphere is expected to correlate with the distribution of surface frost and to collapse on the nightside and in eclipse. In contrast, a volcanic atmosphere should show little diurnal variation and should have strong local density enhancements over active plumes. Arguments in favor of each of the models were given by different observations and different interpretations of the same observations and are explored in-depth by Spencer et al. (2005) and Lellouch et al. (2006).

The ambiguity of the existing observational data in settling the principal question necessitates the development of a detailed computational model of Io's atmosphere that is capable of exploring the relative contributions of the two atmospheric sources. A realistic atmospheric model must use a 3-D domain encompassing the entire planet and must account for the observed distribution of $SO_2$ surface frost and the locations of volcanic plumes. Such a composite (sublimation + plume) model of the $SO_2$ atmosphere using the direct simulation Monte Carlo (DSMC) method for rarefied gas dynamics simulations was developed by Walker et al. (2009).

The sublimation-driven model includes the effects of inhomogeneous $SO_2$ surface frost coverage, diurnal variation of the surface temperature, plasma heating and radiative cooling of the atmosphere. The diurnal surface temperature distribution is based on the model of Saur and Strobel (2004) which is parameterized to produce peak surface temperatures of 115 K or 120 K and a minimum nightside temperature of 90 K (Rathbun et al., 2004). Inhomogeneous surface frosts based on *Galileo* Near Infrared Mapping Spectrometer (NIMS) data (Douté et al., 2001) together with the surface temperature distribution determine the sublimation rate from each surface cell and create inhomogeneous vertical column densities around Io. The peak temperature of surface frost in the model lags the subsolar point by ~30° of longitude which leads to a comparable lag between the peak vertical column density and the subsolar point. Heating of the atmosphere from the bombardment by charged particles from Jupiter's co-rotating plasma torus is modeled via energy flux impinging radially inward from the top of the atmosphere (TOA) and exponentially attenuating as a function of traversed vertical column density. The absorbed plasma energy is assumed to be equally distributed between translational and rotational degrees of freedom of the $SO_2$ molecule and not to affect the vibrational degrees of freedom. However, the vibrational as well as rotational energy states are excited by molecular collisions. The atmospheric cooling is modeled assuming that the atmosphere is optically thin, so the thermal emission by $SO_2$ molecules is either absorbed by the surface or lost to space.

The contribution of volcanoes is accounted for by superimposing pre-computed plumes simulated using the 2-D axisymmetric DSMC method described in Zhang et al. (2003, 2004). Two representative plume types are used: large Pele-type plumes, and smaller Prometheus-type plumes; each of which has day and night versions based on whether the plume is on the dayside or nightside of Io for a given central meridian longitude (CML). The nominal virtual vent conditions of either plume type are chosen to match the observations of shock height and ring radius as discussed in Zhang et al. (2003, 2004). Large volcanoes with ring radii exceeding ~400 km and shock heights of several hundred kilometers are modeled as Pele-type plumes having virtual vent velocities of 900 m/s, temperatures of 650 K and a mass flow rate of $2.6 \times 10^9$ kg/s. Smaller volcanoes with ring radii of ~180 km and a shock height of 120 km are modeled as Prometheus-type plumes having virtual vent velocities of 500 m/s, temperatures of 300 K and a mass flow rate of $1.5 \times 10^9$ kg/s. Two overlapping sets of plume locations were used in the atmospheric model. For the simulation of the Lyman-α images, the locations of active plumes were based on the observations of hot spots with the Keck Adaptive Optics system in the 2–5 μm range (Marchis et al., 2005). In our model, active plumes were placed at the hot spots that were deemed "persistent". For the simulation of the mid-infrared and the millimeter-wave spectra the locations of active plumes were based on the observations of large scale surface changes by the *Galileo* Solid State Imager (SSI) (see Geissler et al., 2004, Fig. 26). In order to superimpose the plumes onto the sublimation atmosphere, the plume and sublimation properties were mass-averaged; for further details on the plume model see Walker et al. (2009, Section 3.7).

The model predicts an asymmetry in the column density distribution relative to the subsolar point, strong circumplanetary flow and non-LTE vertical thermal structure. Depending on the $SO_2$ residence time on the non-frost surface, the sublimation-only model predicts a longitudinal column density asymmetry with higher column abundance on the anti-jovian hemisphere that is attributed to the higher surface frost fraction there. In turn, the composite model predicts an additional column enhancement on the anti-jovian hemisphere which has a higher concentration of volcanic plumes.

Simulations of full disk observations from the atmospheric model implemented on a 3-D spherical grid require the same geometry for the application of a radiative transfer (RT) code. The 3-D spherical-shell RT code *Rassvet*, capable of simulating the remote measurements from an emitting/absorbing and scattering atmosphere with an underlying inhomogeneous emitting/reflecting surface, was developed by Gratiy et al. (2009). The code utilizes the backward photon Monte Carlo (MC) method, which is ideal for simulating observations by detectors having a narrow field of view and can be applied to simulate both disk-integrated spectra and images of the atmosphere. The code is capable of simulating remote measurements over a wide spectral range from millimeter to UV–Vis and can be applied to situations where both thermal emission and reflected/scattered sunlight contribute to the observations.

In this paper we describe the application of *Rassvet* for simulating spectra and images using a 3-D gas dynamic atmospheric model of Io developed by Walker et al. (2009). The simulations correspond to three observations of Io over a wide wavelength range. To our knowledge, this multispectral simulation represents the first attempt at a comprehensive analysis intending to explain observations at different wavelength bands using a single atmospheric model. The outline of the remainder of this paper is as follows. Section 2 introduces the backward MC radiative transfer method and its application to modeling atmospheric radiation.

Simulations of mid-infrared disk-integrated spectra at 19 μm and their comparison to the observations of Spencer et al. (2005) are presented in Section 3. In Section 4, the simulations of disk-resolved images at Lyman-$\alpha$ are presented and their comparison to the HST/STIS data (Roesler et al., 1999; Feaga et al., 2009) are discussed. Section 5 presents the comparison of simulated and observed emission line profiles (Moullet et al., 2008) in the millimeter range and their implications for understanding Io's vertical thermal structure and atmospheric dynamics. The results of the paper are summarized in Section 6.

## 2. The backward Monte Carlo method

When simulating remote observations of planetary atmospheres, we are often concerned with radiation arriving at the detector within a small solid angle. For such problems, the application of a forward photon MC method is neither feasible nor necessary. Rather, the backward method, where photon bundles, the simulated units of the radiation field, are traced in a time-reversed manner from the detector toward the points of emission in the planetary atmosphere, is most advantageous. In this way, all the simulated photon bundles contribute to the remote observation, and radiation which does not reach the field of view of the detector is not simulated at all.

The first application of the backward MC method to the study of light scattering by planetary atmospheres was carried out by Collins and Wells (1970) who developed a 1-D spherical-shell model capable of computing the intensity and polarization of scattered radiation emanating from the top of the atmosphere (TOA) illuminated by the Sun. The backward MC method was put on a rigorous theoretical ground by Walters et al. (1992b) starting from the principle of reciprocity in radiative transfer (e.g. Case, 1957). The first application of the backward MC method to a fully 3-D spherical-shell atmosphere was done by Oikarinen et al. (1999), who modeled sunlight scattered from the Earth's atmosphere into the limb-viewing detector to extract information about atmospheric composition. Gratiy et al. (2009) extended the application of the backward MC method in 3-D spherical-shell geometry to the situations where both thermal emission and scattered sunlight contribute to the observed intensity. They also applied polychromatic ray tracing to the backward MC method, allowing the simulation of remote measurements at several wavelengths simultaneously which results in an improvement of the computational efficiency. Below, the main results of the backward MC method as applied to the simulations of remote measurements from planetary atmospheres are presented following the development of Gratiy et al. (2009).

In the backward MC method, the specific intensity $I_\lambda(\mathbf{r}_d, -\widehat{\mathbf{\Omega}}_d)$ emerging in the direction $-\widehat{\mathbf{\Omega}}_d$ from the top of a radiating atmosphere at $\mathbf{r}_d$, can be found by ejecting $N$ photon bundles from the TOA at $\mathbf{r}_d$ into a reverse direction $\widehat{\mathbf{\Omega}}_d$ as shown in Fig. 1. The trajectory of each individual ray is determined from the appropriate probability density functions (PDF) which depends on the scattering and reflection properties of the atmosphere and surface (Walters and Buckius, 1992a). Each surface element with arbitrary reflectance is represented as a linear combination of perfectly absorbing (black) and perfectly reflecting sub-elements. Upon intersection with a surface from some direction $\widehat{\mathbf{\Omega}}$, a bundle is reflected with the probability equal to the directional–hemispherical reflectance of that element and is absorbed otherwise. This way, each bundle will follow a zig-zag path $l(\mathbf{r})$ as a result of scattering and reflection in the medium until it is lost to space or absorbed by the surface (see Fig. 1). If the bundle is absorbed, its trajectory is terminated and the surface intensity is assigned to the surface effective emission source function $I_{s\lambda}(\mathbf{r}_s, -\widehat{\mathbf{\Omega}}) = B_\lambda(T(\mathbf{r}_s), \widehat{\mathbf{\Omega}}_\odot, -\widehat{\mathbf{\Omega}})$, which generally includes contributions from both the surface thermal emission and the reflected sunlight incident from the direction $\widehat{\mathbf{\Omega}}_\odot$.

Each $i$th path is used to obtain a sample of specific intensity $I^i_\lambda(\mathbf{r}_d, -\widehat{\mathbf{\Omega}}_d)$ measured by the detector in a manner similar to the line-of-sight calculations, except that here the integration is performed along a zig-zag path. If the inhomogeneous, nonisothermal medium is discretized into uniform volume cells, the contribution of the $i$th bundle to the measurement is found as a summation over $M$ cells crossed by the zig-zag path:

$$I^i_\lambda(\mathbf{r}_d, -\widehat{\mathbf{\Omega}}_d) = B_\lambda(T(\mathbf{r}_s), \widehat{\mathbf{\Omega}}_\odot, -\widehat{\mathbf{\Omega}}) \exp(-\tau_\lambda(l_{\max})) + \sum_{m=1}^{M} B_\lambda(T(\mathbf{r}_m), \widehat{\mathbf{\Omega}}_\odot, -\widehat{\mathbf{\Omega}})(\exp(-\tau_\lambda(l_{m1})) - \exp(-\tau_\lambda(l_{m2}))), \quad (1)$$

where $B_\lambda(T(\mathbf{r}_m), \widehat{\mathbf{\Omega}}_\odot, -\widehat{\mathbf{\Omega}})$ is the effective volumetric emission source function, $T(\mathbf{r}_m)$ is the temperature in the $m$th cell, $l_{m2}$ and $l_{m1}$ are the cell boundaries closest to the points of termination and detector, respectively, and $l_{\max}$ is the total path length. The distance $\Delta l_m = l_{m2} - l_{m1}$ that each bundle travels in the $m$th cell can be found by tracing the ray through the computational grid used for the RT calculation. The optical depth $\tau_\lambda(l)$ in Eq. (1) includes only the contribution of absorption and is defined as follows:

$$\tau_\lambda(l) = \int_0^l \kappa_\lambda(\mathbf{r}) dl'(\mathbf{r}), \quad (2)$$

where $\kappa_\lambda(\mathbf{r})$ is the absorption coefficient of the medium. The specific intensity emanating from $\mathbf{r}_d$ can then be found as a statistical average over $N$ samples, obtained by sending out $N$ photon bundles,

$$I_\lambda(\mathbf{r}_d, -\widehat{\mathbf{\Omega}}_d) = \frac{1}{N}\sum_{i=1}^{N} I^i_\lambda(\mathbf{r}_d, -\widehat{\mathbf{\Omega}}_d). \quad (3)$$

## 3. Mid-infrared spectra

In our first application of *Rassvet*, we simulate the disk-integrated 19 μm spectra from the model Io's atmosphere, as it was observed with the TEXES high spectral resolution mid-infrared spectrograph during 2001–2004 (Spencer et al., 2005). The observations are limited to the wavenumber range $\eta = 529$–$531\ \mathrm{cm}^{-1}$ and include at least 16 absorption lines of the $\nu_2$ vibrational band of $SO_2$. The TEXES spectral resolution at these wavelengths, $0.01\ \mathrm{cm}^{-1}$, does not resolve individual lines; nevertheless, blends of unresolved lines in the spectrum provide information about the vertical distribution of atmospheric temperature and gas column. The observations revealed that the depth of the strongest absorption feature, corresponding to the blend of lines centered at $530.42\ \mathrm{cm}^{-1}$, shows a dramatic longitudinal variation in the dayside atmosphere. The band depth relative to continuum, measured with a spectral resolution $R = \eta/\Delta\eta = 57{,}000$, varies from about 1% near longitude 315°W on the sub-jovian hemisphere to 6–7% near longitude 180°W on the anti-jovian hemisphere.

We investigate the fidelity of both sublimation and composite atmospheres with a peak surface temperature of 115 K. Each atmospheric model is examined for two values of the $SO_2$ molecule residence time on a non-frost (rock) surface, which is defined as the mean time a molecule landing on a rock remains stuck to the surface before detaching from it. In the short residence time (SRT) model the mean residence time on a rock surface at 115 K is approximately 5 s (Sandford and Allamandola, 1993), while in the long residence time (LRT) model, representing a highly porous surface (Matson and Nash, 1983), this value is a 1000 times longer. Regardless of the residence time at the surface, the atmospheric

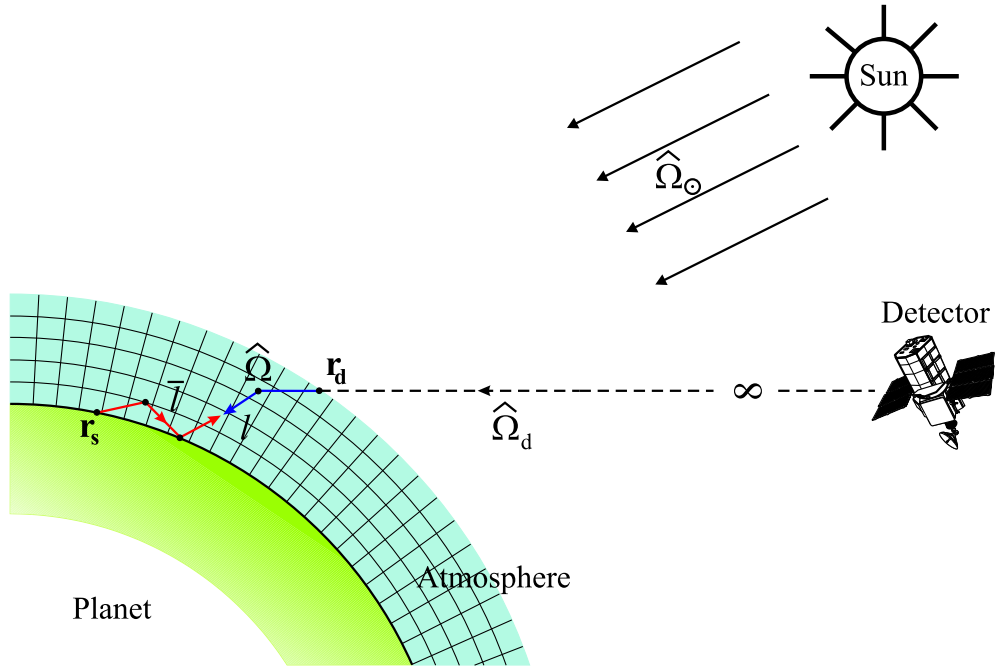


**Fig. 1.** An arbitrary path of a photon bundle through the atmosphere in a backward MC simulation. The bundle ejected from the detector into the direction $\hat{\Omega}_d$ enters the atmosphere at position $\mathbf{r}_d$. The bundle scatters in the atmosphere, reflects from the surface and then scatters again prior to being absorbed by the surface. Bundles may also be lost to space. Also shown is the direction of sunlight $\hat{\Omega}_\odot$.

model manifests a strong longitudinal asymmetry of the column density distribution relative to the subsolar point (Walker et al., 2009, Fig. 14). This asymmetry is caused by the 32° lag of the peak frost temperature relative to the subsolar point resulting in larger column densities on the evening side relative to the morning side. The extent of the column asymmetry along the equator for both short and long residence time models is shown in Fig. 2. In the LRT model the frost-bare surface patches effectively serve as reservoirs for molecules, which are captured for approximately 5000 s before being re-emitted back into the atmosphere. This phenomenon lowers the global sublimation output from the surface and results in lower column densities when compared to the SRT model.

The modeled vertical thermal structure of the atmosphere above the subsolar point is shown in Fig. 3. The translational temperature, equal to the surface temperature at the ground level, monotonically increases with altitude above 1 km as a result of plasma heating. The rotational temperature follows the translational temperature closely up to an altitude of 50 km, above which it departs from LTE. In contrast, the $\nu_2$ vibrational temperature is in strong non-LTE and is everywhere lower than the translational temperature indicating the underpopulation of vibrational levels of $SO_2$. In the rarefied atmosphere of Io this phenomenon is explained by the collisional excitation rate being smaller than the radiative de-excitation rate, resulting in the underpopulation of

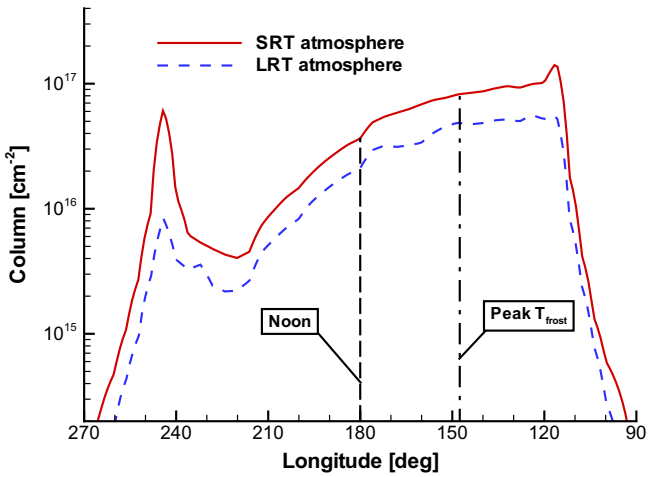


**Fig. 2.** East/west asymmetry in the equatorial line-of-sight column density relative to the noon position (central meridian longitude of 180°W) for the two sublimation models. The asymmetry results from the 32° lag of the frost temperature peak relative to the subsolar point. The peak near the longitude 250° is due to increasing airmass near the limb.

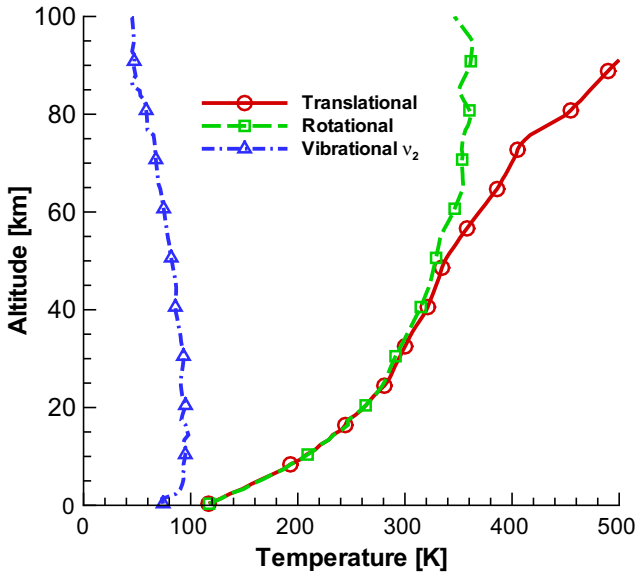


**Fig. 3.** Vertical thermal structure of the atmosphere above the subsolar point for the long residence time model. The vibrational temperature of the $\nu_2$ mode rapidly reaches the non-LTE state and is everywhere lower than the translational and surface temperatures, resulting in absorption spectra.

the vibrational levels and therefore low vibrational temperatures (Walker et al., 2009).

The atmospheric model is utilized to simulate spectra in the narrow wavenumber range $\eta = 530.35–530.45\ cm^{-1}$ containing the 530.42 $cm^{-1}$ absorption feature. The absorption coefficient of $SO_2$ gas is calculated with a high spectral resolution of $2.5 \times 10^6$ using a line-by-line method and adopting the line parameters from Flaud et al. (1993). The surface hemispherical emittances of $SO_2$ (frost) and $S_n$ (a likely non-frost component, see e.g. Geissler et al., 1999) are taken from Nash (1986) and Nash and Betts (1995), who obtained laboratory mid-infrared spectra of these materials. The reported value for the hemispherical emittance at 530.4 $cm^{-1}$ is unity for $SO_2$ frost and 0.8 for solid sulfur. We assume that the hemispherical surface emittance on Io is a linear mixture of the surface components such that $\epsilon = \epsilon_f X_f + \epsilon_n(1 - X_f)$, where $\epsilon_f$ is the emittance of the $SO_2$ frost, $\epsilon_n$ is the emittance of the non-frost, and $X_f$ is the fractional coverage of a surface element by $SO_2$ frost as determined by the NIMS data (Douté et al., 2001). The non-LTE state of the rarefied atmosphere is modeled using a vibrational temperature $T_{v_2}$, provided by the DSMC simulations, in order to calculate the vibrational partition function and the Planck blackbody function. The DSMC model of the atmosphere also provides the distributions of the gas kinetic and rotational temperatures, of the number density of $SO_2$ gas, and of the surface temperature.

In the mid-infrared spectral region, the magnitudes of scattered and surface reflected solar radiation on Io are negligible when compared to the thermally emitted volumetric and surface radiation. Nevertheless, the application of the MC method is still required to model the surface reflection of radiation thermally emitted in the atmosphere. The source functions in Eq. (1) include only the contribution from thermal radiation; thus, the volumetric source is $B_\lambda(T(\mathbf{r}_m), \hat{\mathbf{\Omega}}_\odot, -\hat{\mathbf{\Omega}}) = B_\lambda(T(\mathbf{r}_m))$, and the surface source is $B_\lambda(T(\mathbf{r}_s), \hat{\mathbf{\Omega}}_\odot, -\hat{\mathbf{\Omega}}) = B_\lambda(T(\mathbf{r}_s))$.

The simulations are performed on a spherical grid discretized into $2° \times 2°$ cells corresponding to a spatial resolution better than 63.5 km on the surface, which is much higher than that of any observation of Io's atmosphere. The vertical extent of the atmosphere, modeled up to an altitude of 200 km, is discretized into 20 vertical layers arranged such that each volume cell in a column above a particular surface location contains approximately the same amount of gas. For each subsolar longitude the simulated detector is positioned at the zero phase angle, viewing a fully illuminated dayside atmosphere. To capture the longitudinal variation of band depth we calculate spectra at orbital longitude intervals of 60° corresponding to 60°, 120°, 180°, 240°, 300° and 360°, spanning a full rotation of Io as the satellite revolves around Jupiter. Using the backward MC method, spectra are obtained by ejecting $N = 500$ photon bundles along the parallel lines-of-sight at each of the grid nodes at the TOA for each of 500 simulated wavelengths. The specific intensity reaching the detector is then calculated using the standard backward MC procedure outlined in Section 2. Disk-integrated spectra are found by summing the specific fluxes at the detector from each surface element at the TOA and dividing it by the solid angle subtended by Io as seen from Earth.

To determine which atmospheric model provides the best match to the observations, we calculate the orbital longitudinal variation of the 530.42 $cm^{-1}$ band depth for each atmospheric model. Simulations reveal that the strongest orbital longitudinal variation in band depth among all the examined models occurs for the composite LRT atmosphere whose spectra are shown in Fig. 4. The depicted spectra $I_\eta$ are normalized by the surface continuum $I_c$, and are convolved with a spectral resolution of 57,000 corresponding to that of TEXES. The simulations reproduce the absorption spectral feature seen in the observations of Spencer et al. (2005, see their Figs. 12 and 13) resulting from the fact that

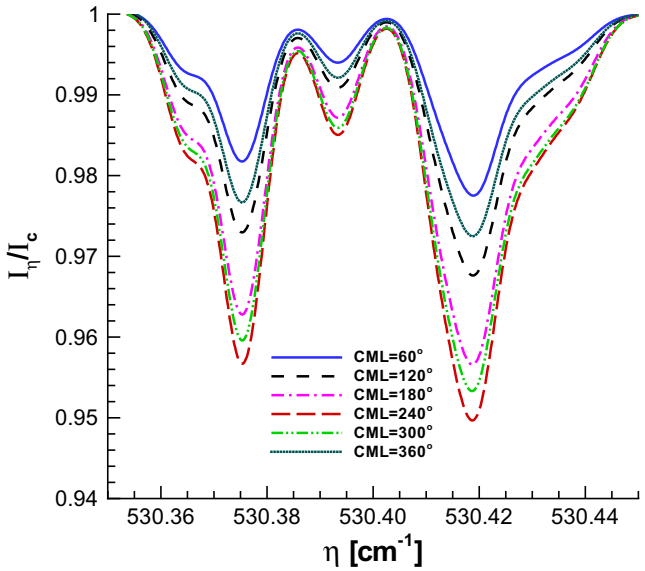


**Fig. 4.** Simulated mid-infrared TEXES spectra calculated from the composite atmospheric model with a long residence time of $SO_2$ on the non-frost surface. The spectrum for each individual surface element was calculated using a line-by-line method, convolved to the resolution of the TEXES spectrograph, and then integrated to produce a single disk-averaged spectrum.

the mean vibrational temperature of the $v_2$ mode of $SO_2$ gas is lower than the surface temperature.

The variation of band depth with orbital longitude obtained from simulated spectra for different atmospheric models and that derived from observations are shown in Fig. 5. The SRT sublimation atmosphere indicates almost no variation of band depth with orbital longitude, despite the longitudinal variation of the surface frost coverage used in the model. This occurs because the column density in this case is almost completely controlled by the surface frost temperature and is negligibly affected by the surface frost fraction (Walker et al., 2009). The vertical thermal structure, in turn, is controlled by the vertical distribution of atmospheric mass, and therefore is also independent of the longitude of the subsolar point. This is clearly indicated in Fig. 6 showing the distribution of line-of-sight column density calculated with ray tracing for the atmospheres with subsolar longitudes of 60° and 240°W. Even though

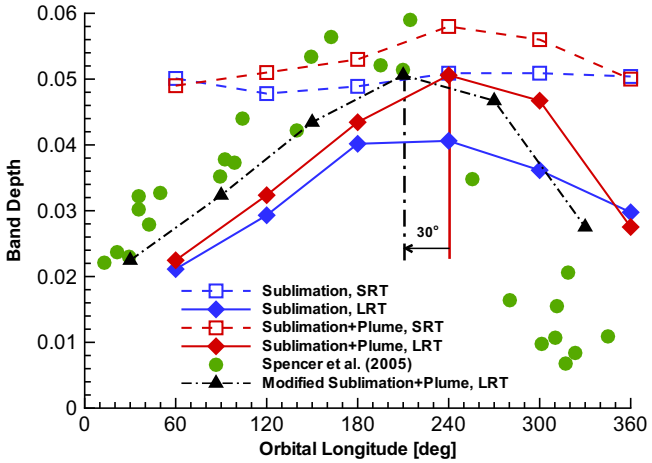


**Fig. 5.** Longitudinal variation of the band depth at 530.42 $cm^{-1}$ derived from simulated spectra for four different atmospheric models and compared to that derived from the spectrum fits of Spencer et al. (2005). Also shown is the modified band depth distribution resulting from a 30° shift in the direction of lower orbital longitudes for the composite LRT model.

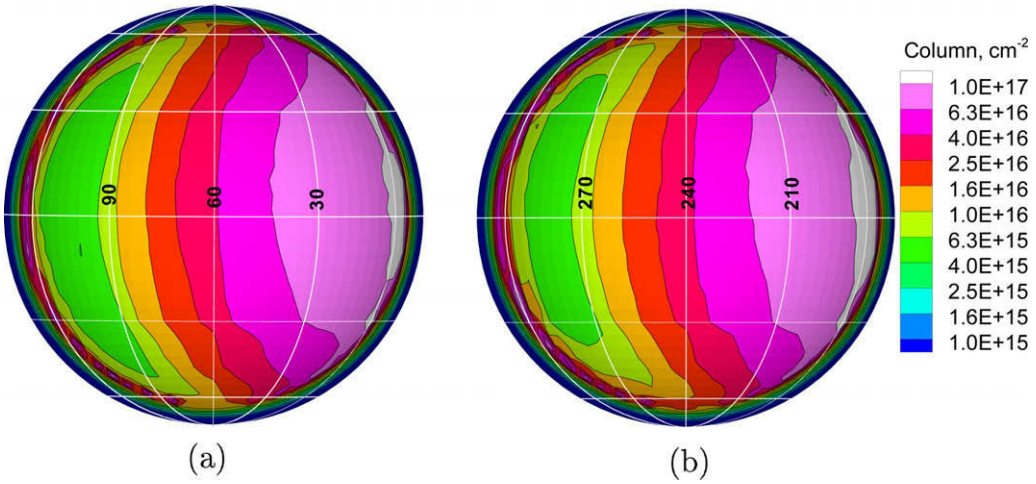


**Fig. 6.** Distribution of the line-of-sight column density for the sublimation atmosphere with short residence time at different longitudes of the subsolar point: (a) at 60° and (b) at 240°W. The column morphology is independent of the surface frost coverage and is controlled purely by the surface temperature distribution.

the vertical column density reaches a maximum ~32° east of the subsolar point on the evening side as shown in Walker et al. (2009, Fig. 14) due to thermal lag, the line-of-sight column density increases monotonically to the east on the evening side as a result of increasing airmass. The column density morphology is virtually the same at different orbital longitudes. This finding is at odds with the observations of Spencer et al. (2005, see their Fig. 14) that are superimposed on Fig. 5 and which indicate a dramatic variation in band depth with the orbital longitude. The observed band depth variation from about 1% near the longitude 315° to 6–7% near the longitude 180°, suggests that the atmosphere of Io supports a thicker column on the anti-jovian hemisphere when compared to the sub-jovian hemisphere. Similar inferences regarding the atmospheric column variation were made from millimeter-wave spectroscopic observations of Lellouch et al. (2000) and Lyman-α imaging of Feaga et al. (2009). However, the observations do not distinguish whether the asymmetry results mainly from the longitudinal variation in the surface frost fraction or in volcanic output.

To find out whether the inclusion of volcanic plumes provides the desired variation in band depth for the SRT model, a composite atmosphere, including both sublimation and plume sources, was used to calculate the longitudinal variation in band depth (see Fig. 5). The spectral simulations show that even though the addition of volcanic plumes results in an increase of the band depth on the anti-jovian hemisphere, where the plumes are predominantly located, it does not result in a decrease in band depth on the sub-jovian hemisphere. Thus, we conclude that neither the composite nor the sublimation SRT atmospheric model provides a satisfactory global model of the atmosphere of Io.

We next investigate the orbital longitudinal band depth variation for the LRT model, in which the residence time of $SO_2$ molecules on rock surfaces is a thousand times longer than that for the SRT model. The lower column densities of the LRT sublimation atmosphere result in weaker absorption of surface thermal radiation and consequently in lower band depth when compared to the SRT model. A more important consequence of increasing the residence time is that in this case frost-bare surface patches capture molecules striking the surface, preventing the lateral diffusion of gas on Io and therefore restricting sublimation to the frost-rich regions. This results in a strong variation in band depth with orbital longitude which correlates with the longitudinal variation of the frost fraction presented by Walker et al. (2009, Fig. 8).

The variation of band depth for the LRT composite atmospheric model provides the best match with the results inferred from the observations by Spencer et al. (2005). The addition of volcanic plumes increases the band depth on the anti-jovian hemisphere with a maximum of 5% at 240°W and suggests the importance of volcanic output for sustaining the global atmosphere on Io. Fig. 7 shows the line-of-sight column density distribution calculated with ray tracing for the orbital longitudes of 60° and 240°W. On the anti-jovian hemisphere, the column is significantly enhanced due to the presence of energetic plumes such as Pele (20.4°S, 256.9°W) and Marduk (27.4°S, 210.4°W), while on the sub-jovian side most of the atmospheric abundance is due to sublimation alone. It appears, that the simulated band depths based on the composite models would have shown much better agreement with the observational data if the former were shifted approximately 30° in the direction of lower orbital longitudes as seen in Fig. 4. This shift is approximately equal to the lag of the peak surface frost temperature relative to the subsolar point in the surface temperature model of Walker et al. (2009, Fig. 3). Since the peak of the frost temperature lags the position of the subsolar point by approximately 32°, frost sublimation occurs predominantly in the region centered at longitudes on Io shifted 32° east of the subsolar point and, therefore, depends on the frost coverage at these lower longitudes. Consequently, the simulated disk-integrated band depth of the sublimation atmosphere at orbital longitude $L$ is determined by the frost coverage of the region centered at Io's longitude of $L$ – 32°. However, if the peak temperature of surface frost occurs with a much smaller lag, sublimation will dominate in the vicinity of the subsolar point and the band depth will be determined by the frost coverage of the region centered at Io's longitude $L$. The variation of band depth with orbital longitude for the latter case approximately corresponds to shifting the calculated band depths 30° in the direction of the lower orbital longitudes, better matching the observations.

This comparison suggests that a strong thermal lag is unlikely to occur on Io prompting a need for a more detailed surface temperature model or a better parameterization of the existing model. A better model can be obtained by solving the 1-D heat conduction equation for each location at the surface undergoing diurnal variation in insolation (Spencer et al., 1989). Such a model would exhibit smaller lags between the peak temperature of surface frost and the subsolar longitude for comparable thermal inertias as used in our model and would better agree with the observations in the Lyman-α.

In an attempt to convert the observed band depths at 530.42 $cm^{-1}$ into equatorial column densities, Spencer et al.

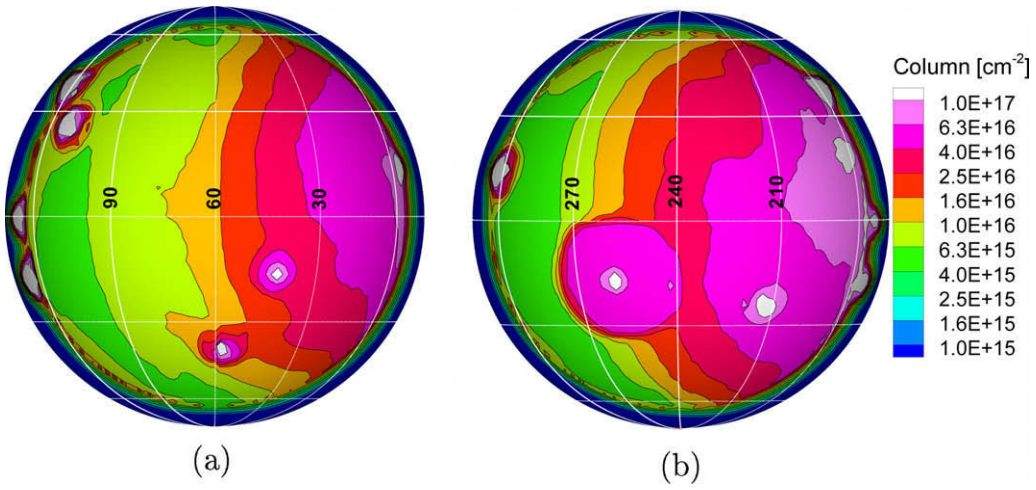


**Fig. 7.** Distribution of line-of-sight column density for the composite atmosphere with long residence time at different longitudes of the subsolar point: (a) at 60° and (b) at 240°W. The column morphology depends on both the surface frost coverage and the locations of volcanic plumes.

(2005) simulated the disk-integrated mid-infrared spectra from four different empirical atmospheric models. Their "modified latitude" model, which assumes an infinite thermal inertia of surface frost and is the most consistent with the latitudinal variation of column densities deduced from HST/STIS observations by Jessup et al. (2004) was preferred for retrieving the atmospheric abundances from band depth data. Even with the horizontal distribution of the atmospheric abundance specified, the equatorial column densities cannot be uniquely inferred, because band depth depends on the distribution of a source function determined by the atmospheric structure and the surface temperature distributions, which also need to be modeled empirically. Moreover, since half of the radiation at 19 μm comes from volcanic hot spots, the observations are weighted toward the atmosphere over these hot spots, which were assumed to be representative of the atmosphere over the rest of the disk by Spencer et al. (2005).

The disk-resolved map of the band depth based on the modified latitude model (see Spencer et al., 2005, Fig. 8) shows no resemblance to the distribution obtained based on the composite LRT model presented in Fig. 8, despite similarities in the longitudinal variation of the disk-integrated band depth in both models. In addition to stronger absorption around the positions of volcanic plumes, the band depth distribution based on the DSMC-modeled atmosphere also shows a significant east/west asymmetry with stronger absorption on the evening side. Even though we concluded that the east/west asymmetry on Io is likely less pronounced than that in the model of Walker et al. (2009), other models of the diurnal surface temperature variation also show a measurable thermal lag of the peak frost temperature relative to the subsolar point (Rathbun et al., 2004, Fig. 7). This invariably leads to a longitudinal column asymmetry for sublimation supported atmospheres, thus excluding the modified latitude model preferred by Spencer et al. (2005) as a valid possibility for the global distribution of the dayside atmosphere of Io. At the same time the DSMC model of Walker et al. (2009) requires a more detailed modeling of the surface temperature in order to better match the observed variation of the band depth with orbital longitude.

## 4. Lyman-α imaging

Even though disk-integrated observations provide important information on the longitudinal variation of column abundance, they are insufficient to reliably constrain the spatial distribution of Io's atmosphere. Different geographic morphologies may result in identical disk-integrated spectra, thus, making the solution of the inverse (retrieval) problem ill-posed. In order to constrain the atmospheric distribution further, disk-resolved far ultraviolet (FUV) observations, which are discussed below, must be considered.

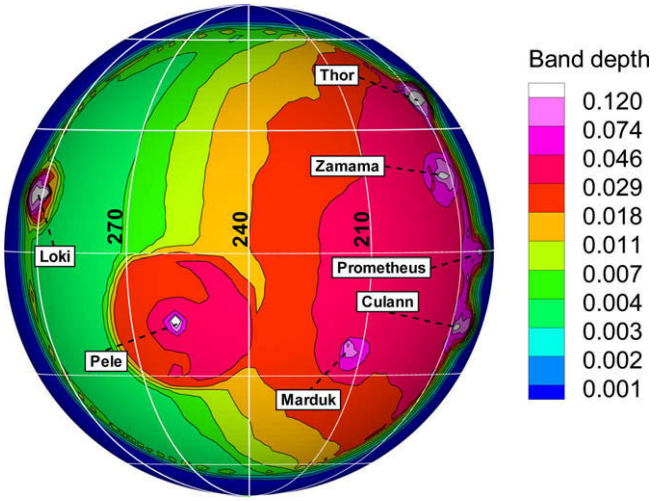


**Fig. 8.** Disk-resolved band depth at 530.42 $cm^{-1}$ for the sunlit hemisphere of Io (central meridian longitude 240°W) at zero phase angle.

The HI Lyman-α images obtained with HST/STIS during 1997–2001, consistently show bright patches with an intensity of ~2 kR located at mid-to-high latitudes with a peak brightness near ±45° and dark regions with an intensity of ~0.7 kR at low latitudes. Feldman et al. (2000) argued that the HST/STIS 1216 Å emission is due to solar Lyman-α radiation that is attenuated by the atmosphere, reflected from the surface, and then further attenuated by the atmosphere before reaching the detector. At 1216 Å, $SO_2$ is a strong continuum absorber with an absorption cross section $\sigma = 3.9 \times 10^{-17}$ $cm^2$ (Manatt and Lane, 1993). Analyzing the 1997–1998 HST/STIS data, Feldman et al. (2000) inferred equatorial/subsolar $SO_2$ column densities on Io in the range of $(1–4) \times 10^{16}$ $cm^{-2}$ decreasing to less than $10^{15}$ $cm^{-2}$ near the poles, with an assumption on the value of the surface Lambert albedo at 1216 Å. Similarly, from the analysis of the HST/STIS image taken on 23 August, 1998, Strobel and Wolven (2001) constructed a model of latitudinal variation of $SO_2$ atmospheric abundance on Io which falls off sharply from $(1–1.7) \times 10^{16}$ $cm^{-2}$ to

about $3 \times 10^{15}$ cm$^{-2}$ beyond ±50° latitude. They also demonstrated that the reflected solar Lyman-α data may well be explained by a volcanically-driven atmosphere with the numerous plumes residing in an equatorial belt below ±30° latitude.

A detailed analysis of the entire HST/STIS Lyman-α dataset was conducted by Feaga et al. (2009) in order to produce a global distribution of Io's $SO_2$ daytime column density. The conversion of Lyman-α brightness distribution to column abundance distribution is complicated by the lack of the direct observations of the surface reflectance of Io at 1216 Å. From observations of the temporal stability of Io's albedo pattern, Feaga et al. (2009) constructed a global reflectance map of Io at Lyman-α based on the correlations between disk-resolved FUV albedo of the trailing hemisphere and near-ultraviolet (NUV) albedo maps at 3460 and 3700 Å that were observed by Sartoretti et al. (1995). Given the surface reflectance map, the atmospheric distribution was then determined by inverting the images of brightness distribution using the Beer–Lambert law (Houghton, 2002). The resulting map reveals a persistent latitudinal fall-off in column density with strong longitudinal asymmetries: on the sub-jovian hemisphere the equatorial column is greater than $1 \times 10^{16}$ cm$^{-2}$ and decreases below $1 \times 10^{15}$ cm$^{-2}$ at latitudes ±25°; whereas on the anti-jovian hemisphere the maximum column density at the equator reaches $5 \times 10^{16}$ cm$^{-2}$ and falls below $1 \times 10^{15}$ cm$^{-2}$ at latitudes ±40°.

### 4.1. FUV surface reflectance

In order to gain a better understanding of the FUV brightness distribution from the surface of Io, we examine the correlations between a map of $SO_2$ surface frost deposits (Douté et al., 2001) and an HST/STIS FUV undispersed image of the trailing hemisphere of Io (Fig. 9a). Acquired on August 23, 1998, at orbital longitude 283.7° with the F25SRF2 filter covering 1280–1780 Å, this is the only such image of Io sampling only the trailing hemisphere. Feaga et al. (2009) estimated that contamination from atomic emission for this image does not exceed 10% in the broadband region, thus concluding that the reflected solar continuum (1500–1780 Å) dominates the image intensity and so allows direct mapping of the FUV reflectance.

It was emphasized by Hapke (1993, p. 191) that low albedo surfaces, such as Io in the FUV, are poorly approximated by Lambert's law. Instead, Hapke's single scattering approximation for bidirectional reflectance provides a much better description of reflectance from low albedo surfaces (Hapke, 1981, 1993). Neglecting the contribution from multiple scattering within the surface grains, Hapke's single scattering approximation for bidirectional reflectance of a surface located at $\mathbf{r}_s$ takes the form

$$r(\mathbf{r}_s, \hat{\mathbf{\Omega}}_\odot, \hat{\mathbf{\Omega}}) = \frac{\omega(\mathbf{r}_s)}{4\pi} \frac{\mu_0(\mathbf{r}_s)}{\mu(\mathbf{r}_s) + \mu_0(\mathbf{r}_s)} (1 + B(\alpha)) P(\alpha), \tag{4}$$

where $\omega(\mathbf{r}_s)$ is the single scattering albedo of the surface, $\mu_0(\mathbf{r}_s)$ and $\mu(\mathbf{r}_s)$ are, respectively, the cosines of incident and reflected rays with the surface normal at $\mathbf{r}_s$, $P(\alpha)$ is the scattering phase function at phase angle $\alpha$ and $B(\alpha)$ is a term that accounts for the opposition effect. The specific intensity reflected from the surface $I(\mathbf{r}_s, \hat{\mathbf{\Omega}})$ in the direction $\hat{\mathbf{\Omega}}$ is then found from

$$I(\mathbf{r}_s, \hat{\mathbf{\Omega}}) = r(\mathbf{r}_s, \hat{\mathbf{\Omega}}_\odot, \hat{\mathbf{\Omega}}) \pi \mathscr{F}, \tag{5}$$

where $\pi\mathscr{F}$ is the incident solar flux.

Following Douté et al. (2001), we will assume that the surface reflectance $r_s(\mathbf{r}_s, \hat{\mathbf{\Omega}}_\odot, \hat{\mathbf{\Omega}})$ at any location on Io can be represented as a linear mixture of surface components such that

$$r_s(\mathbf{r}_s, \hat{\mathbf{\Omega}}_\odot, \hat{\mathbf{\Omega}}) = r_f(\mathbf{r}_s, \hat{\mathbf{\Omega}}_\odot, \hat{\mathbf{\Omega}}) X_f(\mathbf{r}_s) + r_n(\mathbf{r}_s, \hat{\mathbf{\Omega}}_\odot, \hat{\mathbf{\Omega}})(1 - X_f(\mathbf{r}_s)), \tag{6}$$

where $r_f(\mathbf{r}_s, \hat{\mathbf{\Omega}}_\odot, \hat{\mathbf{\Omega}})$ is the reflectance of the $SO_2$ frost, $r_n(\mathbf{r}_s, \hat{\mathbf{\Omega}}_\odot, \hat{\mathbf{\Omega}})$ is the reflectance of non-frost, and $X_f(\mathbf{r}_s)$ is the fractional coverage of a surface element by optically thick $SO_2$ frost.

In the FUV, the surface frost grains are optically thick, rendering volume scattering negligible compared to scattering from the grain surface (Hapke et al., 1981). In this case, the single scattering albedo for each surface component is independent of the grain size. If we further assume that the texture of each surface component is globally uniform, the single scattering albedo becomes independent of position on Io, allowing us to express its bidirectional reflectance as

$$r(\mathbf{r}_s, \hat{\mathbf{\Omega}}_\odot, \hat{\mathbf{\Omega}}) = \frac{\mu_0(\mathbf{r}_s)}{\mu(\mathbf{r}_s) + \mu_0(\mathbf{r}_s)} R(\alpha), \tag{7}$$

where the factor $R(\alpha)$ is a function of phase angle only:

$$R(\alpha) = \frac{\omega}{4\pi}(1 + B(\alpha)) P(\alpha). \tag{8}$$

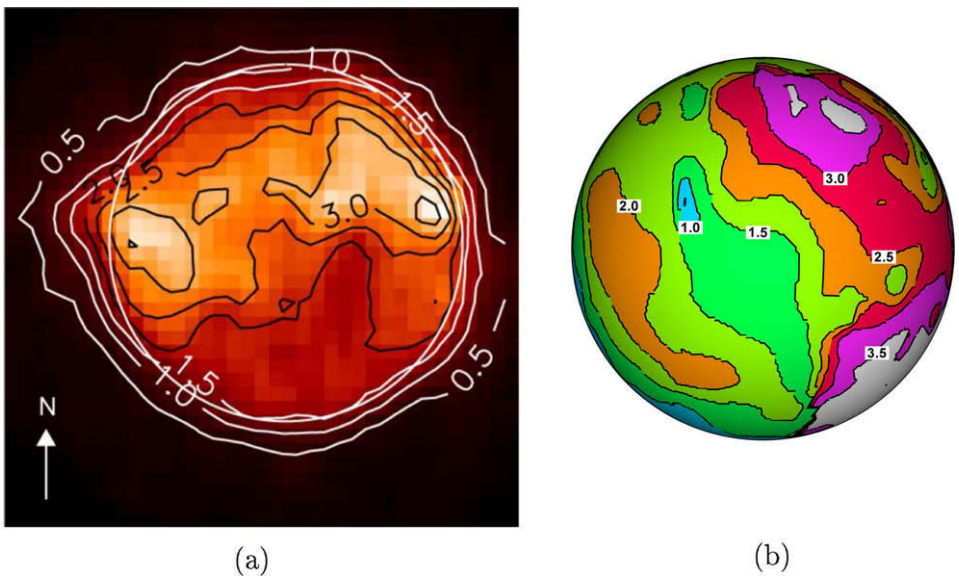


**Fig. 9.** (a) The FUV surface brightness contours in relative units on the trailing hemisphere of Io (Feaga et al., 2009). (b) A map of the product of the frost fraction and Lommel–Seeliger factor corresponding to the conditions of the FUV observation (orbital longitude 283.7° and phase angle $\alpha = 5.05°$). The two maps lack the morphological similarity needed if the FUV surface brightness is correlated with the deposits of the $SO_2$ frost.

Substituting Eq. (7) into Eq. (6) and accounting for the definition of bidirectional reflectance Eq. (5) we obtain the following expression for the distribution of surface brightness:

$$I(\mathbf{r}_s, \widehat{\mathbf{\Omega}}) = \pi \mathscr{F} \frac{\mu_0(\mathbf{r}_s)}{\mu(\mathbf{r}_s) + \mu_0(\mathbf{r}_s)} ((R_f(\alpha) - R_n(\alpha)) X_f(\mathbf{r}_s) + R_n(\alpha)). \quad (9)$$

If the distribution of the $SO_2$ frost fraction $X_f(\mathbf{r}_s)$ inferred by Douté et al. (2001) is predominantly responsible for the variation in the FUV surface brightness $I(\mathbf{r}_s, \widehat{\mathbf{\Omega}})$, then the contour map of the product of the Lommel–Seeliger factor and the frost fraction,

$$\left(\frac{\mu_0(\mathbf{r}_s)}{\mu(\mathbf{r}_s) + \mu_0(\mathbf{r}_s)}\right) X_f(\mathbf{r}_s), \quad (10)$$

on the trailing hemisphere should resemble that of the FUV image on the same hemisphere. Fig. 9 shows the FUV image of the sunlight reflected from Io's trailing hemisphere and a map constructed from Eq. (10) for the geometry of the observation (orbital longitude 283.7° and phase angle $\alpha = 5.05°$). In order to facilitate a comparison between the two maps, the contours of the constructed map were linearly scaled to match the magnitudes of the contours on the FUV image. The two maps show little similarity. The FUV image indicates bright surface patches near both eastern and western limbs at low latitudes, whereas the constructed map results in enhancements near the polar regions, east of the subsolar point. Moreover, the contours of the FUV image indicate an east-to-west elongation, while the contours of the constructed map tend to stretch in a north-to-south direction.

The lack of morphological similarity between the two maps questions the validity of at least one of our main assumptions, namely that the FUV image represents reflected sunlight (Feaga et al., 2009) and that its spatial morphology is correlated with the distribution of $SO_2$ surface frost. Other key assumptions regarding the frost coverage are that the linear mixture represents a valid model for the bidirectional reflectance and that the frost deposits are optically thick (Douté et al., 2001). Rather than addressing each of the above assumptions one-by-one, we emphasize the possibility that the $SO_2$ frost and non-frost may have nearly identical reflectances in the FUV, thus driving the difference $(R_f(\alpha) - R_n(\alpha))X_f$ in Eq. (9) to zero and eliminating the correlation of FUV brightness with frost distribution. In this case, any globally abundant surface contaminant with reflectance different from that of the frost may be responsible for the observed FUV brightness distribution.

### 4.2. Simulated Lyman-α images

To simulate the Lyman-α images we use only the LRT composite atmosphere because it agrees best with the mid-infrared observations described in the previous section. We simulate images for orbital longitudes of 240° and 300°W and compare them to the observations of Feldman et al. (2000, Fig. 2) and Feaga et al. (2009, Fig. 2). Since we are unable to definitively relate the surface frost fraction to the FUV brightness in order to construct the inhomogeneous model of Lyman-α surface reflectance as discussed above, we consider two different models for the unknown surface reflectance. First, we consider a model for which the sunlight scatters only once within the surface grains before leaving the surface. In this case the uniform bidirectional surface reflectance $r$ at the zero phase angle can be found from the geometric albedo $A_p$ using the relationship

$$A_p = \pi r. \quad (11)$$

Analyzing the HST/STIS observations of Io, Feldman et al. (2000) derived a geometric albedo between 1520 and 1700 Å of 1.9% for the 1998 observations and 1.5% for the 1997 observations. Making the assumption that the albedo at 1216 Å is the same as between 1520 and 1700 Å, as suggested by Feldman et al. (2000), we assume that the geometric albedo at the Lyman-α wavelength is fixed at 1.9%. Second, we considered a model in which the bidirectional reflectance obeys Lambert's law

$$r_L = \frac{1}{\pi} A_L \mu_0, \quad (12)$$

with a Lambert albedo $A_L = 0.047$ as was suggested by Strobel and Wolven (2001).

The backward MC simulations of reflected sunlight are conducted in two stages as described in Section 2 of this paper. First, the atmosphere is irradiated with sunlight to determine the effective surface emission source, $B_\lambda(T(\mathbf{r}_s), \widehat{\mathbf{\Omega}}_\odot, -\widehat{\mathbf{\Omega}})$. Then, the backward MC procedure is executed by ejecting $N = 100$ bundles for each pixel at the TOA to find the amount of Lyman-α radiation reflected toward the detector and attenuated in the atmosphere using Eq. (1). Fig. 10 shows four simulated images of Io in the Lyman-α for orbital longitudes of 240° and 300° at the zero phase angle, obtained using the Lambert and single scattering reflectance models. The simulated images manifest magnitudes of disk brightness similar to that seen in the observations; however, the morphology of the brightness distribution across the disk is different. Some of the differences between the observations and simulations can be attributed to a lack of knowledge regarding the surface reflectance distribution at 1216 Å. The application of the Lambert reflectance results in limb darkening apparent from the brightness contours running parallel to the western limb. On the other hand, the application of the uniform reflectance indicates a brightness variation across the disk only due to the variation in the vertical column density and does not manifest any limb darkening. However, unlike the observations, which show a dark equatorial band and polar brightening, the composite model predicts a longitudinal asymmetry in the disk brightness that peaks on the evening side no matter which surface reflectance model is used. This suggests that the variation of the atmospheric column, rather than the surface reflectance variation, dominates the east/west morphology of the Lyman-α images. The morning side brightening results from a longitudinal column asymmetry of the composite atmospheric model with thicker columns on the evening side, as discussed in the analysis of mid-infrared simulations. Thicker atmospheric columns east of the subsolar point make the atmosphere completely opaque to the Lyman-α solar radiation, resulting in dark regions there.

The east/west column asymmetry can be decreased by modifying the surface temperature model by using a two-layer vertical surface frost structure as proposed by Spencer et al. (2005), which would decrease the surface thermal lag. It is much harder to explain other observed features at Lyman-α such as the dark mid-latitude band that is confined to ±45° latitudes and the bright polar regions, neither of which are present on the simulated images. Feaga et al. (2009) attributed the observed latitudinal brightness variation to the sharp fall-off in column density beyond ±45°, with latitudes near ±60° sustaining almost no atmosphere. This inference is at odds with the latitudinal variation of the dayside column density of the sublimation supported atmospheric model of Walker et al. (2009) that is controlled by the surface temperature decreasing as $\cos^{1/4}\theta$ with latitude $\theta$ away from the equator. The latter dependence, however, is commonly used to model the latitudinal variation of the surface temperature (e.g., Ingersoll et al., 1985; Wong and Johnson, 1995) and agrees reasonably well with the observed latitudinal variation of the brightness temperature on Io (Rathbun et al., 2004).

The possibility that the enhanced Lyman-α brightness at high latitudes results from an anomalous surface reflectance at those latitudes is unlikely if we accept that the FUV image of the trailing hemisphere is due to reflected sunlight and if the distribution of surface reflectance between 1520 and 1780 Å is

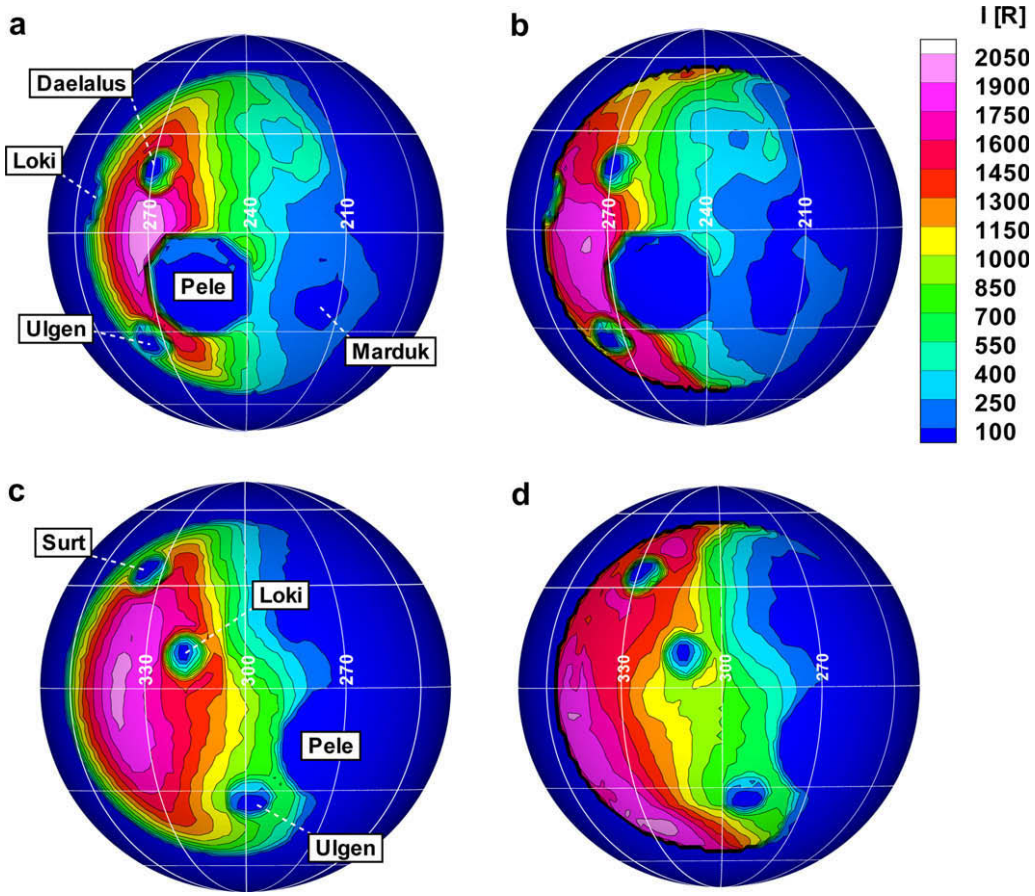


**Fig. 10.** Modeled Lyman-α brightness images of Io (in Rayleighs) at central meridian longitude of 240°W (a and b) and 300°W (c and d). The results are obtained using two different surface reflectance models. (a and c) Lambert surface with $A_L = 0.047$ and (c and d) single scattering approximation of Hapke under the assumption of a linear mixture.

morphologically similar to that at 1216 Å. Indeed, the FUV image indicates that the surface is brighter in the mid-latitude regions and darker in the polar regions. Therefore, unless the surface reflectance morphology at 1216 Å is the inverse of that in the FUV image, the reflectance at high latitudes at Lyman-α will be lower than at mid-latitudes, at least on the trailing hemisphere of Io.

The differences between our model and the observations regarding the latitudinal variation of column abundance invites us to reexamine the possibility that the atmosphere at low latitudes is primarily controlled by volcanism. Strobel and Wolven (2001) estimated that the presence of some 100 plumes of various types and sizes residing at low latitudes could explain the dark equatorial belt in the reflected solar Lyman-α imaging of Io. This number contrasts with the fact that plumes of gas and dust were observed from only 16 different volcanic centers on Io (Lopes et al., 2001). Moreover, smooth geographic variation of daytime $SO_2$ column density within ±40° and ±25° latitude bands on the anti-jovian and sub-jovian hemispheres, respectively, as derived by Feaga et al. (2009, Fig. 13) are difficult to reconcile with the scenario of a volcanic atmosphere that predicts patchy regions on a 100-km scale away from the volcanic vents (Zhang et al., 2003). However, both the estimate of the number of required active plumes and simulations of the extent of the plume atmosphere were made assuming a unit sticking coefficient of the $SO_2$ molecules to the surface. A realistic surface with $SO_2$ frost contamination may have a sticking coefficient significantly smaller than unity. In this case, the number of plumes needed to sustain the observed $SO_2$ atmosphere would be many fewer than 100 as noted by Strobel and Wolven (2001), and the column density enhancement generated by volcanic plumes would have a greater radial extent than that predicted by Zhang et al. (2003), resulting in a smoother variation of the atmospheric column abundance between the plumes.

Alternatively, the correlations between the distribution of daytime $SO_2$ column density and the locations of 157 observed active volcanic hot spots noted by Feaga et al. (2009) suggests that many of the active plumes on Io are "stealth plumes" expelling only the vapor phase and are difficult to detect in sunlight (Johnson et al., 1995). This hypothesis has its own caveat since only two gas plumes, Acala and Culann, which are invisible in daylight, were observed in auroral emissions during eclipse (Geissler and McMillan, 2008). On the other hand, the strong correlation between the locations of surface changes and the spotted plumes, both observed by the *Galileo* SSI between 1996 and 2001, does not eliminate the existence of stealth plumes for two reasons: first, it was concluded by Geissler and McMillan (2008) that the surface changes caused by Prometheus-type plumes are most likely produced by dust rather than by gas deposits, and second, the SSI camera only captures the surface changes at visible wavelengths, for which patches of $SO_2$ frost can appear transparent (Douté et al., 2001). Therefore, both stealth plumes and their $SO_2$ gas deposits may be undetectable by the SSI camera. To this end the quality of the numerical atmospheric model is limited by the lack of more detailed data on the locations and sizes of active plumes and the geographic distribution of the $SO_2$ sticking coefficient.

## 5. Millimeter-wave observations

Lastly, we simulate the disk-integrated $SO_2$ emission line profiles in the millimeter wavelength range from the dayside atmosphere obtained with the single dish IRAM-30 m telescope during October–November 1999. These observations did not resolve the disk of Io and were concentrated around Io's leading (orbital longitude 90°) and trailing (orbital longitude 270°) sides (Lellouch et al., 2006). All detected $SO_2$ lines appear in emission with line contrasts relative to continuum reaching 20–40 K in brightness temperature, implying that the mean gas rotational temperature is higher than the mean surface brightness temperature by at least 20–40 K.

Assuming that the $SO_2$ atmosphere of Io obeys hydrostatic equilibrium, the original interpretation of line emission data by Lellouch et al. (2000) resulted in estimates of mean dayside gas temperatures $T = 400$ K and hemispheric coverage $f_h = 8\%$ on the trailing side and $T = 200$ K and $f_h = 24\%$ on the leading side. The high gas temperature estimates on the trailing side did not support the conclusions of the radiative–conductive model of Strobel et al. (1994), predicting that the gas temperature in the first scale height is lower than 200 K. The addition of a velocity dispersion mechanism within the gaseous plumes contributing to line broadening allowed Lellouch et al. (2006) to fit the observed line profiles with lower temperatures. The trailing side data were then explained with a mean gas temperature of $T = 200$ K covering 30% of the disk, but it required at least 50 active gaseous plumes.

The IRAM-30 m observations obtained in 1999 were reanalyzed by Moullet et al. (2008) based on $SO_2$ spatial distributions of Feaga et al. (2009) and the latitude-dependent model of Spencer et al. (2005). For hydrostatic and isothermal atmospheric model, the line emission data were fit with gas temperatures lower than 200 K, which required scaling the $SO_2$ column density distribution of Feaga et al. (2009) by factors of ~3 and 0.7 on the leading and trailing sides, respectively, and scaling the $SO_2$ column density distribution of Spencer et al. (2005) by the factor of 0.2 on the trailing side. Moreover, in order to obtain a better match with the observed line widths a "super-rotation" of the atmosphere with an equatorial zonal velocity of 170–300 m/s in the prograde direction relative to planetary rotation had to be introduced to create the additional line broadening mechanism.

We simulate disk-integrated spectra of rotational lines at 216.643, 221.965, 251.199 and 251.210 GHz from the dayside hemisphere of Io and compare them to the data acquired with the IRAM-30 m telescope in October–November 1999 (Lellouch et al., 2006). The emission from the leading side is simulated using modeled atmospheres with subsolar longitudes at 60° and 120°W, whereas the emission from the trailing side is simulated using modeled atmospheres with subsolar longitudes at 240° and 300°W. Spectra at the two subsolar longitudes on each side of Io are then averaged to obtain one line profile for both the leading and the trailing hemispheres. The absorption coefficient of $SO_2$ gas is calculated at a high spectral resolution of $4 \times 10^6$ with line parameters obtained from the HITRAN database (Rothman et al., 2004). In order to compare with the observations, the simulated emission profiles are convolved with a Gaussian to the 120 kHz spectral resolution of the data.

The unknown millimeter-wave surface emittance of Io was estimated by requiring that the brightness temperature of the 1.4 mm continuum emission equals 93 and 99 K for the leading and trailing sided, respectively, as determined by Moullet et al. (2008). Assuming a uniform surface emittance and using the surface temperature distribution model of Walker et al. (2009), one finds surface emittances of 0.838 and 0.892 on the leading and trailing sides, respectively, in order to explain the observed continuum brightness temperatures. The backward MC procedure for calculating the disk-integrated spectra from the modeled atmosphere used here is identical to that used for simulating the mid-infrared spectra.

All simulated emission lines are presented in units of brightness temperature, $T_B$, versus velocity, $v = c(\nu - \nu_0)/\nu_0$, where $\nu_0$ is the line center frequency and $c$ is the speed of light. The simulated spectra are then compared to the IRAM-30 m data (Moullet et al., 2008). Fig. 11a shows simulated 216.643 GHz line profiles formed by thermal Doppler broadening on the leading side for both the sublimation and composite LRT atmospheres. The line emission from the sublimation atmosphere exceeds the observed brightness temperature contrasts by 6 K (16% error). It appears that the modeled sublimation atmosphere has an excessive optical depth, which could result from either a higher column abundance or a higher mean rotational temperature. The addition of volcanic plumes to the atmosphere produces an additional 6 K brightness temperature contrast which also could be attributed to an enhanced atmospheric column density and too hot temperature regions in the vicinity of volcanic vents. The disk-resolved absolute brightness temperature maps at the center of the 216.643 GHz line at orbital longitudes of 120° and 240° are shown in Fig. 12. The effect of the plumes is to create stronger emission as a result of hot gas emanating from the vents, thus producing a higher disk-integrated brightness temperature when compared to the sublimation-only model.

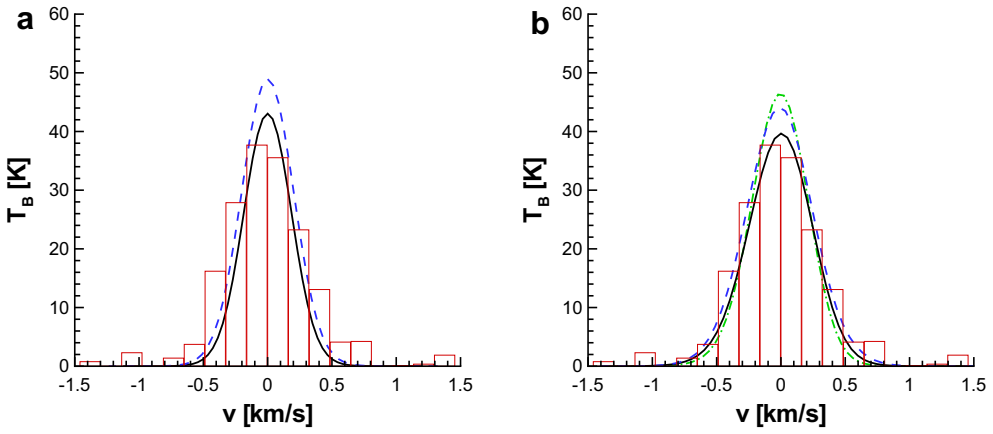


**Fig. 11.** Simulated emission profiles of the 216.643 GHz line on Io's leading side. (a) Line profiles from the sublimation (solid line) and composite (dashed line) atmospheres formed by thermal Doppler broadening alone. (b) Line profiles from the sublimation (solid line) atmosphere with an additional broadening due to circumplanetary flow and composite (dashed line) atmosphere with additional broadening due to both circumplanetary flows and velocity dispersion within the plumes. The case for a composite atmosphere broadened only by the velocity dispersion in the plumes is also presented (dash-dot line). Histograms represent the IRAM-30 m data.

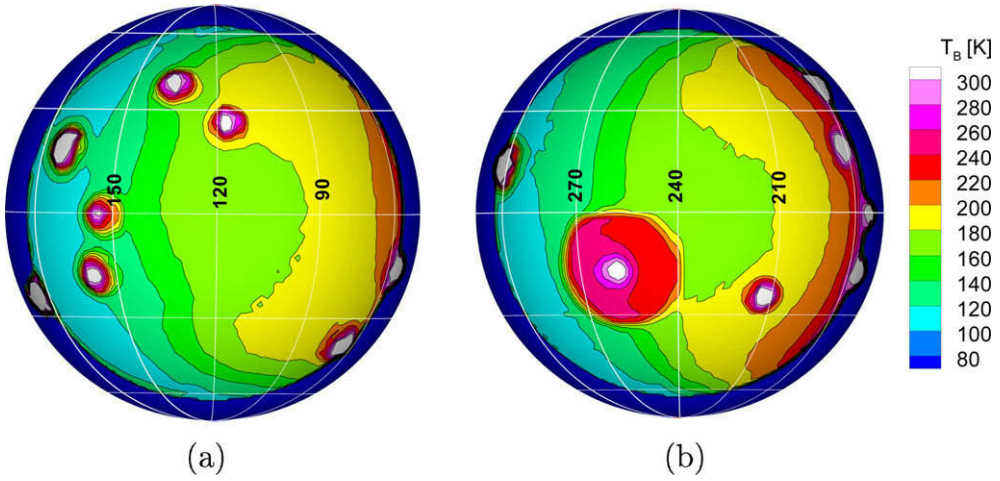


**Fig. 12.** The brightness temperature maps at the center of the 216.643 GHz line for central meridian orbital longitudes of (a) 120° and (b) 240°W.

The simulated line profiles also appear to be too narrow for both models when compared to the IRAM-30 m data. Following Moullet et al. (2008) we examined the contribution of atmospheric dynamics toward broadening of the 216.643 GHz line. The DSMC gas dynamics model includes two effects contributing to the atmospheric motion: day-to-night flows resulting from pressure gradients generated by sublimating gas and volcanic plume expansion. The model, however, does not include atmospheric motion generated by Io's rotation. This contribution can be approximately included by adding a velocity of $V_e \cos\theta$ at latitude $\theta$ to the DSMC model's velocity field, where $V_e = 75$ m/s is the equatorial linear velocity of Io.

Fig. 11b shows the simulated 216.643 GHz line profiles from the leading side for both the sublimation and composite LRT atmospheres where both thermal Doppler effect and atmospheric dynamics contribute to the line broadening. Accounting for the circumplanetary flows and velocity dispersion within the plumes considerably improves the line width match with the IRAM-30 m observations. Moreover, the additional broadening factor favorably reduces the brightness contrast of the simulated lines, which then exceeds the observed values by only 2 and 7 K for the sublimation and composite atmospheres respectively. Fig. 11b also shows the emission line profile for the composite atmosphere for the case where only the velocity dispersion within plumes contributes to the broadening. It is seen that velocity dispersion within the plumes alone, given the modeled vent conditions and the number and the types of volcanic plumes included as a part of the composite atmosphere, is insufficient to produce enough line broadening to be consistent with the IRAM-30 m data.

The Doppler shift map for the composite atmosphere at an orbital longitude of 120° is shown in Fig. 13. Each point on the map represents the line-of-sight velocity component averaged along the atmospheric column. The map indicates strong red shifts of ~300 m/s near the western limb and much weaker blue shifts of ~50 m/s near the eastern limb. Two factors contribute to this limb-to-limb asymmetry of the Doppler shift. Firstly, the day-to-night flow developing in the vicinity of the peak frost temperature accelerates as it travels radially away from the high pressure region but then collapses back to the surface under the influence of gravity near the nightside where the atmosphere becomes sufficiently rarefied. Due to the eastward lag of the peak frost temperature relative to the position of the subsolar point the flow is still accelerating near the eastern limb but collapses in the vicinity of the western limb as shown in Walker et al. (2009, Fig. 7). Secondly, the superimposed solid rotation of the atmosphere reverses the day-to-night flow near the western limb resulting in a blue shift, but also, enhancing the red shift near the eastern limb. The subsolar regions produce blue shifts of ~50 m/s resulting from the

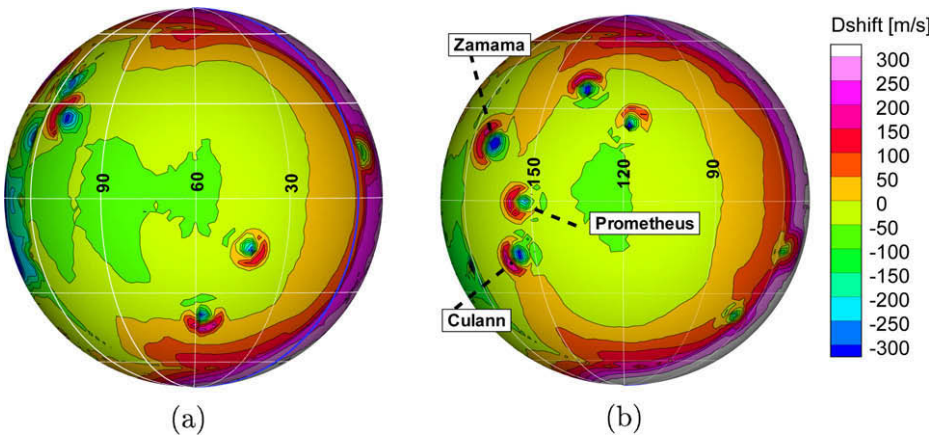


**Fig. 13.** Map of the Doppler shifts on the leading side of Io at central meridian longitudes of (a) 60° and (b) 120°W. Positive velocities indicate red shifts and negative velocities indicate blue shifts. (For interpretation of the references to color in this figure legend, the reader is referred to the web version of this article.)

upward motion of the sublimated gas, whereas plumes are apparent through the much stronger blue shifts of ~300 m/s as a result of hot gas expelling from the volcanic vents.

The modeled Doppler shift map can be compared to that derived from the disk-resolved millimeter-wave observations of Io with the IRAM Plateau de Bure Interferometer (PdBI) in January–February 2005 (Moullet et al., 2008, Fig. 6). The main feature of the measured Doppler shift map is the limb-to-limb velocity difference of 330 ± 100 m/s produced by strong 160 ± 80 m/s red shifts on the western limb and equally strong 170 ± 80 m/s blue shifts on the eastern limb. Provided that the equatorial linear velocity for Io is 75 m/s, Moullet et al. (2008) suggested that the atmosphere may undergo "super-rotation" in the prograde direction with an equatorial zonal velocity of 170–300 m/s. Such strong circumplanetary flows, however, are not predicted either by the current DSMC model or by any previous sublimation-driven models (Ingersoll et al., 1985; Ingersoll, 1989).

Even though our Doppler shift map shows a strong limb-to-limb difference of ~350 m/s, it does not result in strong blue shifts on the eastern limb, as mentioned above. It is possible that the detected approaching winds on the eastern limb are caused by active volcanic plumes (Zamama, Culann, and Prometheus) located at the limb when Io is near its maximum eastern elongation. The modeled Doppler shift distribution in the plumes suggests that the blue shifts are most likely caused by the upwelling portion of the expanding flow rather than horizontal flow below the plume canopy as proposed by Moullet et al. (2008). Although if the plume is located exactly at the limb at the time of observation, the contribution of the upwelling flow is zero.

The angular momentum transfer from the plasma flow impinging on the trailing side of Io with a relative velocity of 57 km/s, was also suggested by Moullet et al. (2008) as another possible mechanism for producing the observed Doppler shifts. On the leading hemisphere this mechanism would result in blue shifts at both limbs, which when combined with strong red shifts at the western limb and weak blue shifts on the eastern limb, as predicted by our DSMC model, can potentially produce the detected Doppler shift map. None of the current atmospheric models of Io, including our DSMC model, account for the momentum transfer from the plasma flow self-consistently. Saur et al. (2002) estimated that the momentum transfer from the plasma is of the same order of magnitude as the gravitational acceleration and hence should decrease the atmospheric scale height upstream and increase it downstream. Clearly then, the momentum transfer from the plasma should also effect the circumplanetary winds. If subsequent observations verify the detected Doppler shifts, the inclusion of momentum transfer from the plasma flow could drastically change our understanding of the atmospheric dynamics on Io.

Since the inclusion of modeled atmospheric motion as an additional broadening factor improved the line width of the 216.643 GHz line, all subsequent spectra are calculated accounting for circumplanetary flows and velocity dispersion within the plumes. Fig. 14 shows simulated line profiles of the 252 GHz doublet from the trailing hemisphere, whereas Fig. 15 shows the simulated line profiles of the 221.965 GHz line on both leading and trailing sides. Comparison of simulated spectra with IRAM-30 m observations shows a similar pattern to that noted for the 216.643 GHz line. The line widths for all lines match the IRAM-30 m observations well, but the line contrasts of the simulated spectra are too strong. The largest difference occurs for the 251.199 GHz line where the simulated brightness contrast exceeds the observations by 7 and 10 K for the sublimation and composite atmospheres, respectively.

It would be premature to argue that the above comparison favors the sublimation-only atmosphere of Io, since different factors such as having a poor surface temperature model or a lack of detailed data on the sticking coefficient of $SO_2$, among several others, can contribute to the possible discrepancy in the brightness temperature contrasts. For example, the emission line contrasts are largely determined by the gradients of the vertical thermal structure in the atmosphere, with stronger gradients producing stronger line contrasts. The DSMC-modeled vertical thermal profile shown in Fig. 3 indicates a strong temperature gradient of 8 K/km in the first scale height, causing the atmospheric temperature to rise above 200 K at an altitude of 10 km. These results exceed the prediction of the radiative–conductive model of Strobel et al. (1994) which concludes that the solar and plasma heated atmosphere reaches temperatures of 200 K at altitudes greater than 30 km. Thus, if vertical thermal gradients on Io, within the first few scale heights where most of the emission takes place, are smaller than those predicted by our DSMC model, the simulated emission line profiles will result in smaller brightness temperature contrasts for the same disk column distribution.

## 6. Conclusion

This paper describes simulations of spectra and images from the 3-D gas dynamics model of the atmosphere of Io using the backward MC radiative transfer code *Rassvet*. Simulations are performed for sublimation and composite atmospheric models for

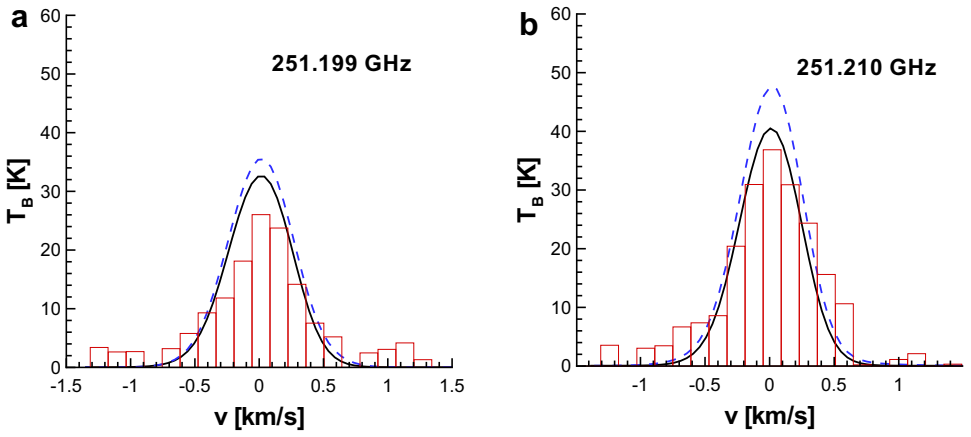


**Fig. 14.** Simulated emission profiles of 252 GHz doublet on the trailing side from sublimation (solid line) and composite (dashed line) atmospheres with circumplanetary flow and velocity dispersion in the plumes. Histograms represent the IRAM-30 m data.

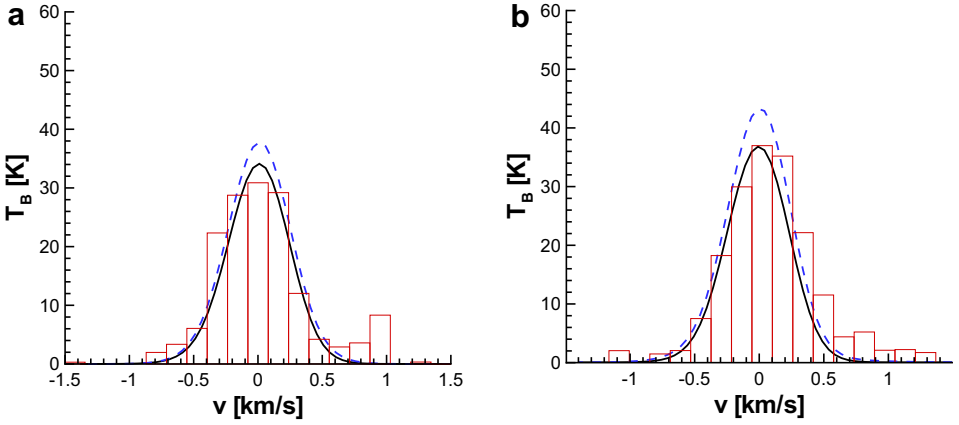


**Fig. 15.** Simulated emission profiles of the 221.965 GHz line from sublimation (solid line) and composite (dashed line) atmospheres with circumplanetary flow and velocity dispersion in the plumes. (a) Leading hemisphere and (b) trailing hemisphere. Histograms represent the IRAM-30 m data.

two different values of the $SO_2$ molecule residence time on a non-frost surface. Simulations of disk-integrated mid-infrared spectra with the short residence time indicates almost no longitudinal variation in band depth for the 530.42 $cm^{-1}$ feature, which is not supported by the observations of Spencer et al. (2005). On the other hand, the composite atmosphere with a long residence time provides a much better match with the observations, indicating a $SO_2$ gas column enhancement on the anti-jovian hemisphere. Both the longitudinal variation of the surface frost fraction and of the plume density contribute to the column enhancement on the anti-jovian side, suggesting the importance of both plume and sublimation sources for supporting the atmosphere. It was found that much better agreement with the mid-infrared data would occur if the simulated variation of band depth with orbital longitude for the composite atmosphere was shifted $\sim 30^\circ$ in the direction of the lower orbital longitudes. Such a modified composite atmosphere would result if the surface of Io had a much smaller effective thermal inertia than that used in the model of Walker et al. (2009), leading to a much smaller lag between the positions of the maximum surface temperature and the subsolar point. A more accurate modeling of the surface temperature distribution on Io would require the application of a diurnal conductive model of the heat flow underneath the surface. Such a model is currently being developed based on the thermophysical model of Spencer et al. (1989).

Assuming that the surface reflectance on Io can be represented as a linear mixture of its components and that the surface deposits are optically thick, we examined the correlation between the HST/STIS FUV image of the trailing hemisphere and the map of the surface frost fraction. We argued that if the FUV brightness is due to reflected sunlight and if its spatial morphology depends on the distribution of $SO_2$ frost, then we should find a correlation between the image brightness and the distribution of the surface fraction scaled by the Lommel–Seeliger factor. The lack of such a correlation between the two maps prohibits construction of a simple FUV surface reflectance model which is based on the distribution of the surface frost fraction and suggests that the reflected FUV image brightness distribution may be due to the distribution of a globally abundant surface contaminant.

Comparison of simulated images at Lyman-$\alpha$ to the data (Feldman et al., 2000; Feaga et al., 2009) shows strong morphological differences. The bright polar regions, which are consistently observed at all orbital longitudes, suggest that Io's atmosphere is confined to an equatorial band of $\theta = \pm 45^\circ$ latitude. This data is difficult to explain within the framework of the sublimation-driven model of Walker et al. (2009) producing appreciable sublimation rates at mid-latitudes and thus sustaining a thick atmosphere there. Unlike the simulated image, the HST/STIS Lyman-$\alpha$ observations do not show a strong east/west brightness asymmetry, suggesting that the line-of-sight column density distribution on Io is nearly symmetric relative to the central meridian. This conclusion is similar to that made from the analysis of the mid-infrared data and suggests that the value of the thermal inertia of the surface layer on Io is much lower than that used in the surface temperature model of Walker et al. (2009).

When only the thermal Doppler effect contributes to line broadening, simulated millimeter-wave disk-integrated emission line profiles for the long residence time atmospheres are too narrow in comparison to the IRAM-30 m data. However, inclusion of an additional broadening mechanism due to atmospheric winds considerably increases the line widths and reduces the excess brightness contrasts of the simulated emission profiles, providing much better agreement with the data. The additional broadening is explained by a strong limb-to-limb velocity difference of 350 m/s resulting from asymmetries of the day-to-night flow of the sublimated gas relative to the subsolar position. Similar strong limb-to-limb velocity differences are reported by PdBI observations but show peculiar strong blue shifts on the eastern limb which are not predicted by our gas dynamics model. Unless these blue shifts are caused by gas expelled from several volcanic plumes coincidentally located near the eastern limb during the PdBI observation of the leading hemisphere or the plasma momentum transfer, the need to explain the observed blue shifts may significantly change our understanding of physical processes driving atmospheric dynamics on Io.

## Acknowledgments

This research was supported by NASA Planetary Atmospheres Grant, NNG05GO83G. The large portion of DSMC computations at UTA were performed at the Texas Advanced Computing Center. We are grateful to Emmanuel Lellouch for providing us with correct line parameters for $SO_2$ gas and to Arielle Moullet for sharing the IRAM-30 m telescope data with us. We are also thankful to the anonymous referees for many detailed and helpful suggestions to this paper.

## References

Case, K.M., 1957. Transfer problems and the reciprocity principle. Rev. Mod. Phys. 29 (4), 651–663.

Collins, D.G., Wells, M.B., 1970. FLASH, a Monte Carlo procedure for use in calculating light scattering in spherical shell atmospheres. Rep. RRA-T704, Radiation Research Associates, Inc., Fort Worth, Texas.

Douté, S., Schmitt, B., Lopes-Gautier, R., Carlson, R., Soderblom, L., Shirley, J., 2001. Mapping $SO_2$ frost on Io by the modeling of NIMS hyperspectral images. Icarus 149 (1), 107–132.

Feaga, L.M., McGrath, M., Feldman, P.D., 2009. Io's dayside $SO_2$ atmosphere. Icarus 201 (2), 570–584.

Feldman, P.D., Strobel, D.F., Moos, H.W., Retherford, K.D., Wolven, B.C., McGrath, M.A., Roesler, F.L., Woodward, R.C., Oliversen, R.J., Ballester, G.E., 2000. Lyman-$\alpha$ imaging of the $SO_2$ distribution on Io. Geophys. Res. Lett. 27 (12), 1787–1790.

Flaud, J.M., Perrin, A., Salah, L.M., Lafferty, W.J., Gauelachvili, G., 1993. A reanalysis of the (010), (020), (100), and (001) rotational levels of $^{32}S^{16}O_2$. J. Mol. Spectrosc. 160 (1), 272–278.

Geissler, P.E., McMillan, M.T., 2008. Galileo observations of volcanic plumes on Io. Icarus 197 (2), 505–518.

Geissler, P.E., McEwen, A.S., Keszthelyi, L., Lopes-Gautier, R., Granahan, J., Simonelli, D.P., 1999. Global color variations on Io. Icarus 140 (2), 265–282.

Geissler, P.E., McEwen, A.S., Phillips, C., Keszthelyi, L., Spencer, J., 2004. Surface changes on Io during the Galileo mission. Icarus 169 (1), 29–64.

Gratiy, S.L., Levin, D.A., Walker, A.C., 2009. Rassvet: Backward Monte Carlo radiative transfer in spherical-shell planetary atmospheres. Icarus 207 (1), 394–408.

Hapke, B., 1981. Bidirectional reflectance spectroscopy. I. Theory. J. Geophys. Res. 86, 3039–3054.

Hapke, B., 1993. Theory of Reflectance and Emittance Spectroscopy, first ed. Cambridge University Press, p. 191.

Hapke, B., Wells, E., Wagner, J., Partlow, W., 1981. Far-UV, visible, and near-IR reflectance spectra of frosts of $H_2O$, $CO_2$, $NH_3$ and $SO_2$. Icarus 47 (3), 361–367.

Houghton, J.T., 2002. The Physics of Atmospheres, third ed. Cambridge University Press, pp. 9–12.

Ingersoll, A.P., 1989. Io meteorology: How atmospheric pressure is controlled locally by volcanos and surface frosts. Icarus 81 (2), 298–313.

Ingersoll, A.P., Summers, M.E., Schlipf, S.G., 1985. Supersonic meteorology of Io: Sublimation-driven flow of $SO_2$. Icarus 64 (3), 375–390.

Jessup, K.L., Spencer, J.R., Ballester, G.E., Howell, R.R., Roesler, F., Vigel, M., Yelle, R., 2004. The atmospheric signature of Io's Prometheus plume and anti-jovian hemisphere: Evidence for a sublimation atmosphere. Icarus 169 (1), 197–215 (Special issue: Io after Galileo).

Johnson, T.V., Matson, D.L., Blaney, D.L., Veeder, G.J., Davies, A., 1995. Stealth plumes on Io. Geophys. Res. Lett. 22, 3293–3296.

Lellouch, E., Belton, M., De Pater, I., Paubert, G., Gulkis, S., Encrenaz, T., 1992. The structure, stability, and global distribution of Io's atmosphere. Icarus 98 (2), 271–295.

Lellouch, E., Paubert, G., Strobel, D.F., Belton, M., 2000. Millimeter-wave observations of Io's atmosphere: The IRAM 1999 compaign. Bull. Am. Astron. Soc. 32 (1), 3511.

Lellouch, E., McGrath, M.A., Jessup, K.L., 2006. Io's atmosphere. In: Lopes, R.M.C., Spencer, J.R. (Eds.), Io After Galileo. Springer, pp. 231–264.

Lopes, R.M.C., and 10 colleagues, 2004. Lava lakes on Io: Observations of Io's volcanic activity from Galileo NIMS during the 2001 fly-bys. Icarus 169 (1), 140–174.

Manatt, S.L., Lane, A.L., 1993. A compilation of the absorption cross-sections of $SO_2$ from 106 to 403 nm. J. Quant. Spectrosc. Radiat. Trans. 50 (3), 267–276.

Marchis, F., and 11 colleagues, 2005. Keck AO survey of Io global volcanic activity between 2 and 5 μm. Icarus 176 (1), 96–122.

Matson, D.L., Nash, D.B., 1983. Io's atmosphere: Pressure control by regolith cold trapping and surface venting. J. Geophys. Res. Space Phys. 88, 4471–4783.

McGrath, M.A., Belton, M.J.S., Spencer, J.R., Sartoretti, P., 2000. Spatially resolved spectroscopy of Io's Pele plume and $SO_2$ atmosphere. Icarus 146 (2), 476–493.

Morabito, L.A., Synnott, S.P., Kupferman, P.N., Collins, S.A., 1979. Discovery of currently active extraterrestrial volcanism. Science 204 (4396), 972.

Moullet, A., Lellouch, E., Moreno, R., Gurwell, M.A., Moore, C., 2008. First disk-resolved millimeter observations of Io's surface and $SO_2$ atmosphere. Astron. Astrophys. 482, 279–292.

Nash, D.B., 1986. Mid-infrared reflectance spectra (2.3–22 μm) of sulfur, gold, KBr, MgO, and halon. Appl. Opt. 25, 2427–2433.

Nash, D.B., Betts, B.H., 1995. Laboratory infrared spectra (2.3–23 μm) of $SO_2$ phases: Applications to Io surface analysis. Icarus 117 (2), 402–419.

Oikarinen, L., Sihvola, E., Kyrölä, E., 1999. Multiple scattering radiance in limb-viewing geometry. J. Geophys. Res. Atmos. 104 (D24), 31–261.

Pearl, J., Hanel, R., Kunde, V., Maguire, W., Fox, K., Gupta, S., Ponnamperuma, C., Raulin, F., 1979. Identification of gaseous $SO_2$ and new upper limits for other gases on Io. Nature 288, 757–758.

Rathbun, J.A., Spencer, J.R., Tamppari, L.K., Martin, T.Z., Barnard, L., Travis, L.D., 2004. Mapping of Io's thermal radiation by the Galileo photopolarimeter–radiometer (PPR) instrument. Icarus 169 (1), 127–139.

Roesler, F.L., Moos, H.W., Oliversen, R.J., Woodward Jr., R.C., Retherford, K.D., Scherb, F., McGrath, M.A., Smyth, W.H., Feldman, P.D., Strobel, D.F., 1999. Far-ultraviolet imaging spectroscopy of Io's atmosphere with HST/STIS. Science 283 (5400), 353–356.

Rothman, L.S., and 29 colleagues, 2005. The HITRAN 2004 molecular spectroscopic database. J. Quant. Spectrosc. Radiat. Trans. 96 (2), 139–204.

Sandford, S.A., Allamandola, L.J., 1993. The condensation and vaporization behavior of ices containing $SO_2$, $H_2S$, and $CO_2$: Implications for Io. Icarus 106 (2), 478–488.

Sartoretti, P., McGrath, M.A., McEwen, A.S., Spencer, J.R., 1995. Post-Voyager brightness variations on Io. J. Geophys. Res. Planets 100 (E4), 7523–7530.

Saur, J., Strobel, D.F., 2004. Relative contributions of sublimation and volcanoes to Io's atmosphere inferred from its plasma interaction during solar eclipse. Icarus 171 (2), 411–420.

Saur, J., Neubauer, F.M., Strobel, D.F., Summers, M.E., 2002. Interpretation of Galileo's Io plasma and field observations: I0, I24, and I27 flybys and close polar passes. J. Geophys. Res. Space Phys. 107 (A12), 1422.

Spencer, J.R., Lebofsky, L.A., Sykes, M.V., 1989. Systematic biases in radiometric diameter determinations. Icarus 78 (2), 337–354.

Spencer, J.R., Lellouch, E., Richter, M.J., López-Valverde, M.A., Lea Jessup, K., Greathouse, T.K., Flaud, J.M., 2005. Mid-infrared detection of large longitudinal asymmetries in Io's $SO_2$ atmosphere. Icarus 176 (2), 283–304.

Strobel, D.F., Wolven, B.C., 2001. The atmosphere of Io: Abundances and sources of sulfur dioxide and atomic hydrogen. Astrophys. Space Sci. 277 (1), 271–287.

Strobel, D.F., Zhu, X., Summers, M.E., 1994. On the vertical thermal structure of Io's atmosphere. Icarus 111 (1), 18–30.

Walker, A.C., Gratiy, S.L., Levin, D.A., Goldstein, D.B., Varghese, P.L., Trafton, L.M., Moore, C.H., Stewart, B., 2009. A comprehensive numerical simulation of Io's sublimation-driven atmosphere. Icarus 207 (1), 409–432.

Walters, D.V., Buckius, R.O., 1992a. Monte Carlo methods for radiative heat transfer in scattering media. Annu. Rev. Heat Trans. 5, 131–176.

Walters, D.V., Buckius, R.O., 1992b. Rigorous development for radiation heat transfer in nonhomogeneous absorbing, emitting and scattering media. Int. J. Heat Mass Trans. 35, 3323–3333.

Wong, M.C., Johnson, R.E., 1995. The effect of plasma heating on sublimation-driven flow in Io's atmosphere. Icarus 115 (1), 109–118.

Zhang, J., Goldstein, D.B., Varghese, P.L., Gimelshein, N.E., Gimelshein, S.F., Levin, D.A., 2003. Simulation of gas dynamics and radiation in volcanic plumes on Io. Icarus 163 (1), 182–197.

Zhang, J., Goldstein, D.B., Varghese, P.L., Trafton, L., Moore, C., Miki, K., 2004. Numerical modeling of Ionian volcanic plumes with entrained particulates. Icarus 172 (2), 479–502.